

A New, Efficient Stellar Evolution Code for Calculating Complete Evolutionary Tracks

Attay Kovetz^{1,2*}, Ofer Yaron^{2*} and Dina Prialnik^{2*}

¹*School of Physics and Astronomy, Sackler Faculty of Exact Sciences, Tel Aviv University, Israel*

²*Department of Geophysics and Planetary Sciences, Sackler Faculty of Exact Sciences, Tel Aviv University, Israel*

31 October 2018

ABSTRACT

We present a new stellar evolution code and a set of results, demonstrating its capability at calculating full evolutionary tracks for a wide range of masses and metallicities. The code is fast and efficient, and is capable of following through all evolutionary phases, without interruption or human intervention. It is meant to be used also in the context of modeling the evolution of dense stellar systems, for performing live calculations for both normal star models and merger-products.

The code is based on a fully implicit, adaptive-grid numerical scheme that solves simultaneously for structure, mesh and chemical composition. Full details are given for the treatment of convection, equation of state, opacity, nuclear reactions and mass loss.

Results of evolutionary calculations are shown for a solar model that matches the characteristics of the present sun to an accuracy of better than 1%; a $1 M_{\odot}$ model for a wide range of metallicities; a series of models of stellar populations I and II, for the mass range 0.25 to $64M_{\odot}$, followed from pre-main-sequence to a cool white dwarf or core collapse. An initial final-mass relationship is derived and compared with previous studies. Finally, we briefly address the evolution of non-canonical configurations, merger-products of low-mass main-sequence parents.

Key words: stars: evolution – Hertzsprung-Russell (HR) diagram – stars: interiors – stars: general – methods: numerical.

* E-mails: attay@etoile.tau.ac.il (Kovetz); oferya@post.tau.ac.il (Yaron); dina@planet.tau.ac.il (Prialnik)

1 INTRODUCTION

Simulating the evolution of a star requires the solution of a set of partial differential equations with boundary conditions at the center and surface, involving extensive input physics, such as equations of state, nuclear reactions, opacities, as well as recipes for treating convection, mass loss, or material mixing. This is accomplished by complex computer codes that are time consuming and depend on a large number of adjustable parameters, both physical and numerical, needed for dealing with evolutionary phases that are different in nature. From the formation to the death of a star, differences between evolutionary phases are so large, that studies are usually devoted to—and often codes are devised for—a specific part of a star’s life, ignoring or simplifying, or suppressing others. So far, no code has been suited or applied to obtain complete, unabridged evolutionary tracks over the entire range of stellar masses and metallicities, although many have come close to accomplishing this task (e.g. Pols et al. 1995, Pols et al. 1998). For example, most (if not all) evolution codes crash at the helium core flash phase. Most of the stellar evolution codes do not solve simultaneously for the structure and the composition; this introduces serious errors in some critical phases whenever the mass grid $\{m_i\}$ changes, as it must eventually (Stancliffe 2006). Our aim has been to develop a versatile and robust stellar evolution code that is free of such handicaps.

A further demand on the code is efficiency and speed. Furthermore, it should be capable not only of evolving any star through all phases without intervention, but also of dealing with peculiar objects. Such a code could be incorporated into an N-body code that deals with dense stellar systems, if not at present, then—given the rapid and continual advance in computing power—in the foreseeable future. The computation methods of N-body gravitating systems have undergone a revolutionary development owing to the work of Aarseth (1963) (see review by Aarseth 1999) and gaining impetus in the past two decades (e.g. Heggie & Hut 2003, Hurley et al. 2001, Hurley et al. 2005): not only have new algorithms been developed, capable of dealing with dense stellar systems (e.g. Portegies Zwart et al. 2001, Portegies Zwart et al. 2004), but also special hardware has been constructed under the GRAPE (GRAvity PipE) project (Makino et al. 1997).

However, in order to render these sophisticated N-body calculations realistic, the effect of the structure and evolution of the constituent stars must be considered as well. This led, less than a decade ago, to the development of the MODEST (MOdelling DENSE STellar systems) project, whose aim is to combine N-body dynamics with the hydrodynamics of

stellar collisions on the one hand, and with stellar evolution of the cluster population, on the other (see Hut et al. (2003)). So far, studies of stellar systems have resorted to short cuts based on sets of discrete pre-calculated evolutionary tracks: either interpolating between them, or using parametrized fit formulae. Clearly, this procedure is incapable of dealing with ‘non-canonical’ stars, the outcome of collisions and mergers.

In this paper we thus present a new evolutionary code that we have developed with this aim in mind. The outline of the code and method of solution are presented in the next section, Section 2; the input physics is described in some detail in Section 3, and results of representative calculations are discussed in Section 4.

2 THE EVOLUTION CODE

2.1 Set of Equations and Boundary Conditions

The equations that govern the evolution of a star are those of continuity, hydrostatic equilibrium, energy transfer (radiative or convective), energy balance, and composition balance:

$$\frac{\partial}{\partial m} \frac{4\pi}{3} r^3 = \frac{1}{\rho}, \quad (1)$$

$$\frac{\partial p}{\partial m} = -\frac{Gm}{4\pi r^4}, \quad (2)$$

$$\frac{\partial \ln T}{\partial m} = \nabla \frac{\partial \ln p}{\partial m}, \quad (3)$$

$$\frac{\partial u}{\partial t} + p \frac{\partial}{\partial t} \frac{1}{\rho} = q - \frac{\partial L}{\partial m}, \quad (4)$$

$$F_j = -\sigma_j \frac{\partial Y_j}{\partial m}, \quad (5)$$

$$\frac{\partial Y_j}{\partial t} = R_j - \frac{\partial F_j}{\partial m}. \quad (6)$$

In these equations, mass m and time t are the independent variables. The dependent ones are radius r , density ρ , temperature T , and the number fractions Y_j , related to the mass fractions X_j by $Y_j = X_j/A_j$, where A_j is the j ’th atomic mass. The particle flux F_j of the j ’th species is assumed to be diffusive (proportional to the abundance gradient of the j ’th species), determined by the diffusion coefficient σ_j .

We regard (ρ, T, Y) as the basic thermodynamic variables. They determine, through the equation of state, the pressure $p(\rho, T, Y)$ and the specific energy $u(\rho, T, Y)$, as well as the opacity $\kappa(\rho, T, Y)$, energy production rate $q(\rho, T, Y)$ and nuclear energy rates $R_j(\rho, T, Y)$ (via an imported list of tables and formulae). The temperature ‘gradient’ $\nabla(r, L, m, \rho, T, Y)$ and

the (convective mixing) diffusion coefficients $\sigma_j(r, L, m, \rho, T, Y)$ are provided by convection recipes.

The foregoing equations are to be solved subject to the following boundary conditions: at the centre,

$$r = 0, \quad L = 0, \quad F_j = 0 \quad ; \quad (7)$$

at the surface, which we take to be the stellar photosphere,

$$\kappa p_G = (1 - \Gamma) g \tau_s, \quad L = 4\pi r^2 \sigma T^4, \quad F_j = 0 \quad . \quad (8)$$

In the first member of eq. (8), p_G is the material ('gas') pressure which, together with the radiation pressure p_R , makes up the total p ; $\Gamma = \kappa L / 4\pi c G m$; $g = Gm/r^2$; and τ_s is the photospheric optical depth, which we take to be unity (Kovetz 1998, Kovetz 1999).

We shall solve the equations of evolution over a grid of mass points $m_1 = 0, m_2, \dots, m_n = M$, but we shall follow (Eggleton 1971, Eggleton 1972) in using an *adaptive* grid, where the mass points m_2, \dots, m_{n-1} depend on the solution. Since, by eqs. (1)–(2), r at the centre varies like $m^{1/3}$, and p like $m^{2/3}$, we replace m by $x = m^{2/3}$, and r by $s = r^2$, in this pair of equations. Equations (1)–(6) then become

$$ds = \frac{3}{4\pi\rho} \left(\frac{x}{s}\right)^{\frac{1}{2}} dx \quad , \quad (9a)$$

$$d \ln p = -\frac{3G}{8\pi p} \left(\frac{x}{s}\right)^2 dx \quad , \quad (9b)$$

$$d \ln T = \nabla d \ln p \quad , \quad (9c)$$

$$dL = \left[q - \frac{\delta u + p \delta \frac{1}{\rho}}{\delta t} \right] dm \quad , \quad (9d)$$

$$F_j = -\sigma_j \frac{dY_j}{dm} \quad , \quad (9e)$$

$$dF_j = \left(R_j - \frac{\delta Y_j}{\delta t} \right) dm \quad . \quad (9f)$$

These may be regarded as differential equations, written in terms of differentials; alternatively, they may be thought of as representing difference equations. In the latter case, at the centre, the indeterminate ratio $x/s = 0/0$ is replaced by its limit $(4\pi\rho_1)/3)^{2/3}$, where ρ_1 is the central value of the density. The change from r to s obviously requires appropriate changes (such as $s = 0, g = Gm/s$) in the boundary conditions.

The equations of structure and composition are solved simultaneously with a mass distribution function, implementing an adaptive mesh. This is done by requiring constant in-

crements of a monotonic function of the form

$$f = (m/M)^{2/3} + c_1 X_H - c_2 \ln p - c_3 \ln \frac{T}{T + c_4}, \quad (10)$$

where the c 's are appropriate non-negative constants. Near the centre the requirement of equal increments of f will lead to equal increments of $x = m^{2/3}$. The second term of f will force equal increments of the hydrogen mass fraction where X_H changes rapidly (at an H-burning shell). The third will lead to equal steps of $\ln p$ towards the surface, where $m/M \approx 1$ and X_H is uniform; and the last term will cause a fine subdivision around $T = c_4 \approx 20,000K$, where the opacity varies rapidly over several orders of magnitude.

2.2 Numerical Scheme

The variables $(s, m, L, \rho, T, p, Y_j)$ are represented by arrays over a grid of $i = 1, \dots, n$, where $i = 1$ corresponds to the centre, and $i = n$ to the surface (photosphere). Thus eqs. (9a)–(9b) become the difference equations

$$s_i - s_{i-1} = \frac{1}{2} \left[\frac{3}{4\pi\rho_{i-1}} \left(\frac{x_{i-1}}{s_{i-1}} \right)^{1/2} + \frac{3}{4\pi\rho_i} \left(\frac{x_i}{s_i} \right)^{1/2} \right] (x_i - x_{i-1}) \quad , \quad (11)$$

$$\ln p_i - \ln p_{i-1} = -\frac{1}{2} \left[\frac{3G}{8\pi p_{i-1}} \left(\frac{x_{i-1}}{s_{i-1}} \right)^2 + \frac{3G}{8\pi p_i} \left(\frac{x_i}{s_i} \right)^2 \right] (x_i - x_{i-1}) \quad . \quad (12)$$

There is one such pair of equations for each $i = 2, \dots, n$. Together with the boundary conditions $s_1 = 0$ and $(\kappa p_G)_n = (1 - \Gamma_n)g_n\tau_s$, these add up to $2n$ equations.

The variables ∇ , L and F_j , related to the energy and particle fluxes, are replaced by arrays that refer to the *midpoints* $i \pm 1/2$. Thus eqs. (9c)–(9f) become

$$\ln T_i - \ln T_{i-1} = \nabla_{i-\frac{1}{2}}(\ln p_i - \ln p_{i-1}) \quad , \quad (13)$$

$$L_{i+\frac{1}{2}} - L_{i-\frac{1}{2}} = \left[q_i - \frac{\delta u_i}{\delta t} - p_i \frac{\delta \frac{1}{\rho_i}}{\delta t} \right] \frac{1}{2}(m_{i+1} - m_{i-1}) \quad , \quad (14)$$

$$F_{i+\frac{1}{2}} = -\sigma_{i+\frac{1}{2}} \frac{Y_{i+1} - Y_i}{m_{i+1} - m_i} \quad , \quad (15)$$

$$F_{i+\frac{1}{2}} - F_{i-\frac{1}{2}} = \left(R_i - \frac{\delta Y_i}{\delta t} \right) \frac{1}{2}(m_{i+1} - m_{i-1}) \quad . \quad (16)$$

where, in the last pair of equations, we have suppressed the index j that refers to the nuclear species. The coefficients $\nabla_{i-\frac{1}{2}}$ and $\sigma_{i+\frac{1}{2}}$ are evaluated by using the arithmetic means of the grid-point arguments, for example $r_{i-\frac{1}{2}} = (r_{i-1} + r_i)/2$. Again, there is one eq. (13) for each $i = 2, \dots, n$, which, together with the boundary condition $L_n = 4\pi r_n^2 \sigma T_n^4$, brings the number of equations up to $3n$. Furthermore, there is one set of eqs. (14) and (16) for each $i = 1, \dots, n$ (and for each one of the species). If J is the number of species, the number of

equations becomes $(4 + J)n$. At $i = 1$ we set $L_{i-\frac{1}{2}} = F_{i-\frac{1}{2}} = 0$ and $m_{i-1} = 0$ in eqs. (14) and (16), which takes care of the central boundary conditions $L = F = m = 0$. At $i = n$ we set $L_{i+\frac{1}{2}} = L_n$, $F_{i+\frac{1}{2}} = 0$ and $m_{i+1} = m_n$ in eqs. (14) and (16). This is in accord with the surface boundary conditions.

The requirement of equal increments of the mesh function f is simply

$$f_{i+1} - f_i = f_i - f_{i-1}. \quad (17)$$

There is one such equation for each $i = 2, \dots, n - 1$. At the ends $i = 1$ and $i = n$ we respectively impose the two boundary conditions

$$m_1 = 0, \quad m_n = M + \dot{M}\delta t, \quad (18)$$

where $\dot{M}(m_n, r_n, L_n)$ is the rate of mass accretion—or loss, if negative. Thus we have a total of $(5 + J)n$ equations for $(5 + J)n$ variables—5 arrays (s, L, m, ρ, T) and J arrays Y_j , each array being of length n .

The partial time derivatives, $\partial u(m, t)/\partial t$, etc., have been replaced, respectively, by difference ratios $\delta u/\delta t$, etc. When a configuration at a previous time is available, δu is usually taken to be $u(m, t) - u(m, t - \delta t)$, where $u(m, t)$ is iterated upon. The solution of eqs. (9a)–(9f) then has the accuracy $O(\delta t)$. It should be noted that $u(t - \delta t)$ is represented by a grid function over a (previous) set of m_i 's that will not generally include the m for which $u(m, t - \delta t)$ is desired. We therefore determine $u(m, t - \delta t)$ by interpolation, using cubic Hermite splines. These splines have the advantage that, if the grid function vanishes at two consecutive m_i 's, the interpolant will not dip below zero anywhere between them. This is especially important when interpolating the number fractions Y_j .

Except at the first time step, the previous, as well as the anteprevious, configurations are available. Instead of a chord through $u(m, t)$ and $u(m, t - \delta t)$, we can then pass a *parabola* through $u(m, t)$, $u(m, t - \delta t)$ and $u(m, t - \delta t - \delta t')$, and evaluate its derivative at t . If this derivative is again denoted by $\delta u/\delta t$, we have

$$\delta u = \alpha u(m, t) + \beta u(m, t - \delta t) + \gamma u(m, t - \delta t - \delta t'), \quad (19)$$

where

$$\alpha = \frac{\delta t' + 2\delta t}{\delta t' + \delta t}, \quad \beta = -\frac{\delta t' + \delta t}{\delta t'}, \quad \gamma = \frac{(\delta t)^2}{(\delta t' + \delta t)\delta t'}. \quad (20)$$

This leads to a solution with accuracy $O(\delta t^2)$. Of course $u(m, t - \delta t - \delta t')$, like $u(m, t - \delta t)$, has to be determined by interpolation.

The $(5 + J)n$ nonlinear eqs. (11)–(18) for the the arrays (s, L, m, ρ, T, Y_j) are solved

simultaneously by Newton-Raphson iterations. This requires, at each iteration stage, the solution of a linear system with a band matrix of order $(5 + J)n$, and band width $15 + 4J$.

The derivatives required by the Newton-Raphson method are evaluated analytically whenever possible. In the case of opacities, which are obtained from tables with the aid of cubic Hermite spline interpolation, we use the (analytic) derivatives of the splines. Numerical derivatives are only used for the energy generation and loss rates, because the neutrino loss rates are provided by cumbersome fit formulae.

2.3 Computational Details

Our automatically varying timesteps, determined mainly by limits imposed on the maximal changes (a few percent), and on the number of Newton-Raphson iterations, allowed during a timestep, span a wide dynamic range—from seconds/minutes during core or shell flashes to several times 10^8 or even 10^9 years in the main-sequence phase (of low-mass stars). With a relative accuracy of ~ 0.0001 , the typical number of Newton-Raphson iterations is 3–4. The grid mass shells, determined by the mass-distribution function, span a range of $\sim 10^{-15} M_\odot$ (in a WD atmosphere) to $\gtrsim 10^{-1} M_\odot$ (in an inert stellar core). There is an option of fixing the mass grid, which we are forced to use during the WD cooling phase, when the mass array $\{m_i\}$ ceases to be monotonically increasing in double precision arithmetic. With these features in mind, the typical number of grid points may be as low as 150 or 200; a typical number of timesteps for a complete evolutionary track is 1000; and typical execution time is of the order of 10 (± 5) minutes on a portable computer (Pentium 4 and higher). The latter is, however, strongly dependent on both physical behaviour (e.g. mass-loss rate or the amount of evolutionary phases taking place) and computational prescriptions (required outputs/interfaces).

The code—targeted for Unix/Linux machines—is written in Fortran 90 and consists of an online graphical interface using Tim Pearson’s PGPLOT.

3 INPUT PHYSICS

3.1 Equation of State (EOS)

The EOS is derived from a free energy, which is a sum of ionic, radiative and electronic contributions, together with corrections for pressure ionization, Coulomb interactions and quantum effects:

$$\begin{aligned}
F &= \sum_i F(T, V, N_i) - \frac{1}{3}aT^4V \\
&\quad + \Omega(T, V, \mu_F) + (\mu_F - mc^2)N \\
&\quad + F_{PI} + F_{CQ}.
\end{aligned} \tag{21}$$

where V is the volume, a is Stefan-Boltzmann's constant, μ_F is the Fermi chemical potential, and m is the electron's mass. The free energy of the N_i particles of the i 'th ionic species is

$$\begin{aligned}
F(T, V, N_i) &= (kT \ln \frac{N_i}{z_i} - kT + \chi_i)N_i, \\
z_i &= VQ_i \ell_i^{-3}, \quad \ell_i = \frac{h}{\sqrt{2\pi m_i kT}},
\end{aligned} \tag{22}$$

where χ_i is the reference energy (relative to the completely ionized state) of the i 'th ion, and Q_i is its partition function. The thermal length ℓ_i depends on the temperature and on the i 'th particle's mass $m_i = A_i m_H$, where A_i is the atomic or molecular weight.

We take account of ionization equilibria for hydrogen and helium; heavier elements (the 'metals') are assumed to be completely ionized. In the stellar envelope, where the metals amount to at most a few percent by mass, and a few thousandths by number, this introduces an error that is much smaller than other uncertainties in the EOS. In a carbon/oxygen stellar core, the metals are pressure-ionized in any case. Ionization equilibria of the metals play an important role in determining the opacity, but we use opacity tables that are entirely independent of our EOS.

Remembering that the reference energies for the completely ionized species H^+ and He^{++} are zero by definition, the χ_i for H , H_2 , H^+ , He , He^+ and He^{++} are, respectively, -13.598, -31.673, 0, -79.003, -54.416 and 0 (in eV). Also, $\chi_i = 0$ for the metals.

Except for the case of H_2 , we replace the partition function Q_i by a constant statistical weight g_i , which is 1 for H^+ , He , He^{++} and all metals, and 2 for H and He^+ . For the hydrogen molecule, we use our own table of $Q_{H_2}(T)$, which we have calculated, using the molecular constants of Tatum (1966); see also Irwin (1987).

Electrons and positrons are described by the fermion grand thermodynamic potential

$$\Omega(T, V, \mu_F) = -Cmc^2V \int_{\beta}^{\infty} \Gamma(\epsilon/\beta) D_+(\epsilon, \phi) d\epsilon/\beta, \tag{23}$$

where

$$\begin{aligned}
 C &= \frac{1}{\pi^2} \left(\frac{mc}{\hbar} \right)^3, & \Gamma(x) &= \frac{1}{3}(x^2 - 1)^{\frac{3}{2}}, \\
 D_{\pm}(\epsilon, \phi) &= \frac{1}{e^{\epsilon - \phi} + 1} \pm \frac{1}{e^{\epsilon + \phi} + 1}, \\
 \beta &= \frac{mc^2}{kT}, & \phi &= \frac{\mu_F}{kT},
 \end{aligned} \tag{24}$$

(Rakavy et al. 1967). The Fermi chemical potential μ_F , which includes the rest-mass energy, is connected with the number *difference*, electrons minus positrons, through

$$\begin{aligned}
 N &= -\Omega_{\mu_F}(T, V, \mu_F) \\
 &= CV \int_{\beta}^{\infty} \Gamma'(\epsilon/\beta) D_{-}(\epsilon, \phi) d\epsilon/\beta = N_e - N_p,
 \end{aligned} \tag{25}$$

where $\Omega_{\mu_F}(T, V, \mu_F)$ denotes the partial derivative $\partial\Omega(T, V, \mu_F)/\partial\mu_F$. Clearly the positron contribution, which is due to the second term of D_{\pm} , becomes insignificant whenever ϕ is large (say $\phi \geq 15$). The last equation determines $\mu_F(T, V, N)$ as a function of T , V and N (actually the Fermi parameter $\epsilon_F = (\mu_F - mc^2)/kT$ in terms of T and N/V). The number difference N must satisfy the equation of charge neutrality

$$N = \sum Z_i N_i. \tag{26}$$

If, in the expression (21) for the free energy, electrons appeared only in the second line, then it would follow that

$$\begin{aligned}
 F_N(T, V, N) &= \Omega_{\mu_F} \mu_{F,N} + \mu_{F,N} N + \mu_F - mc^2 \\
 &= \mu_F - mc^2,
 \end{aligned} \tag{27}$$

where the subscript N denotes the partial derivative with respect to N , at constant T and V . Thus μ_F would indeed be the electron chemical potential $\mu = F_N + mc^2$. We maintain the distinction (between μ and μ_F) because other parts of the free energy—for example the pressure ionization term F_{PI} —too, depend on the electron number density.

The pressure $p = -F_V$, the entropy $S = -F_T$ and their derivatives require derivatives of Ω , with respect to β or ϕ , up to the second order. This leads to five additional Fermi-Dirac integrals, in which $\Gamma(\epsilon/\beta)$ is replaced by $\Gamma'(\epsilon/\beta)$, $(\epsilon/\beta)\Gamma'(\epsilon/\beta)$, $\Gamma''(\epsilon/\beta)$, $(\epsilon/\beta)\Gamma''(\epsilon/\beta)$ or $(\epsilon/\beta)^2\Gamma''(\epsilon/\beta)$. In the degenerate case, when $\epsilon_F = \phi - \beta > 5$, Ω is calculated by Sommerfeld's method, and then differentiated. Otherwise the six integrals involving the first, electronic, part of D_{\pm} are calculated in one swoop, using Gaussian quadrature. The nodes and weights for this quadrature are calculated at the beginning of the run, and their number can be chosen by the user (the code's default is 12 nodes). The positronic contribution, which is

due to the second part of D_{\pm} , is then obtained by using the same procedure, with ϕ replaced by $-\phi$. The last step is only carried out when $\phi < 15$; otherwise, positrons are ignored.

The pressure ionization term in the free energy is taken from Pols et al. (1995):

$$\begin{aligned} F_{PI} &= -N_e kT g(n_e, T) + N_{e0} kT g(n_{e0}, T), \\ g(n_e, T) &= e^{-(c_1/x)^{c_2}} [y + \epsilon_F + c_3 \ln(1 + x/c_4)], \\ x &= n_e m_H, \quad n_e = N_e/V, \quad y = 13.60/kT, \\ (c_1, c_2, c_3, c_4) &= (3, 0.25, 2, 0.03), \end{aligned} \tag{28}$$

where the 13.60 is in eV, and the units of c_1 and c_4 are g cm^{-3} . Furthermore, N_{e0} is the total number of electrons, bound or free, and $n_{e0} = N_{e0}/V$. The object of F_{PI} is to induce pressure ionization by reducing the electronic chemical potential as the number of electrons $n_e a_0^3$ in a cube with side a_0 , the Bohr radius, increases. Of course F_{PI} tends to zero as ionization becomes complete, that is, as $N_e \rightarrow N_{e0}$.

The last term, F_{CQ} , in the free energy depends on the Coulomb parameter Γ and on the Debye parameter Λ . For a one-component plasma (OCP)

$$\Gamma_i = \frac{Z_i^2 e^2}{r_i kT}, \tag{29}$$

where Z_i is the atomic number, e is the electron charge and $r_i = (4\pi N_i/3V)^{-1/3}$ is the ion-sphere radius. For a mixture, we replace this by

$$\Gamma = \frac{\sum X_i Z_i^2/A_i}{\sum X_i Z_i/A_i} \left[\left(\frac{\sum X_i Z_i/A_i}{\sum X_i/A_i} \right)^2 \frac{4\pi n_e}{3} \right]^{1/3} \frac{e^2}{kT}, \tag{30}$$

where the sums refer to a fully ionized plasma mixture with mass fractions X_i . Again, for a one component plasma,

$$\Lambda_i = \frac{\hbar\omega_{pi}}{kT}, \quad \omega_{pi}^2 = \frac{4\pi Z_i^2 e^2 n_i}{m_i}, \tag{31}$$

where ω_{pi} is the plasma frequency. For a mixture, we replace this by

$$\Lambda = \frac{\hbar\omega_p}{kT}, \quad \omega_p^2 = \left(\sum X_i Z_i/A_i \right) N_A 4\pi e^2 n_e, \tag{32}$$

where N_A is Avogadro's number. The expression for F_{OCP} takes different forms for the gas-liquid and for the solid phases, and is based on the work of Iben et al. (1992). Noting that the OCP form of the translational part (that is, setting $Q_i = 1$ and omitting the χ_i 's) of the ionic free energy $\sum F(T, V, N_I)$ is

$$\begin{aligned} \frac{F^0}{\sum N_i kT} &= 3 \ln \Lambda - 1.5 \ln \Gamma + \frac{1}{2} \ln \frac{\pi}{6} - 1 \\ &= 3 \ln \Lambda - 1.5 \ln \Gamma - 1.32351, \end{aligned} \tag{33}$$

Iben et al. (1992) write the OCP free energies in the form

$$\left(\frac{F_{\text{OCP}}}{\sum N_i kT}\right)_{\text{liq}} = 3 \ln \Lambda - 1.5 \ln \Gamma - 1.32351 - H_l(\Gamma) + J(\Lambda), \quad (34)$$

$$\left(\frac{F_{\text{OCP}}}{\sum N_i kT}\right)_{\text{sol}} = \frac{F_{\text{vib}}}{\sum N_i kT} - H_s(\Gamma), \quad (35)$$

where $J(\Lambda)$ takes care of the quantum effects in the gas-liquid phase,

$$\begin{aligned} H_l &= \frac{\sqrt{3}}{3} \Gamma^{3/2} + \Gamma^3(-0.104584 \\ &\quad + 0.172110 \ln \Gamma - 0.033724 \Gamma^{3/2}), & \Gamma \leq 1, \\ H_l &= 0.897744 \Gamma - 3.801720 \Gamma^{1/4} + 0.758240 \Gamma^{-1/4} \\ &\quad + 0.814871 \ln \Gamma + 2.584778, & 1 \leq \Gamma \leq 200, \\ H_s &= 0.895929 \Gamma + \frac{1612.5}{\Gamma^2}, \end{aligned} \quad (36)$$

and $F_{\text{vib}}(\Lambda)$ is the vibrational contribution to the free energy (Kovetz & Shaviv 1970). Iben et al. (1992) have shown that $F_{\text{vib}}/\sum N_i kT$ can be fitted by a weighted sum of two Debye free energies:

$$\frac{F_{\text{vib}}}{\sum N_i kT} = \alpha L\left(\frac{\Lambda}{\Lambda_1}\right) + (1 - \alpha)L\left(\frac{\Lambda}{\Lambda_2}\right), \quad (37)$$

where $\alpha = 0.5711$, $\Lambda_1 = 1.0643$, $\Lambda_2 = 2.9438$, and $L(x)$ is given by

$$L(x) = \frac{9}{8}x + 3 \ln(1 - e^{-x}) - D(x), \quad D(x) = \frac{3}{x^3} \int_0^x \frac{t^3 dt}{e^t - 1}. \quad (38)$$

The function $J(\Lambda)$ is known (Shaviv & Kovetz 1972) to have the the high-temperature limit $\Lambda^2/12$. At low temperatures the OCP liquid should resemble a bcc lattice, with the ions vibrating about their equilibrium positions. This leads to a $J(\Lambda)$ proportional to Λ : according to Iben et al. (1992), $J(\Lambda) \rightarrow 1.06980\Lambda$ (although their foregoing fit for F_{vib} yields $F_{\text{vib}} \rightarrow 0.76758\Lambda$). They then suggest a functional form for $J(\Lambda)$ that interpolates between these limits. But this leads to a non-monotonic entropy (T-derivative of the gas-liquid F_{OCP}); in particular, the specific heat has the required T^3 dependence at low T , but with the wrong sign!

Rather than adopt Iben et al.'s $J(\Lambda)$, we note that, for $\Lambda \ll 1$, $F_{\text{vib}}/\sum N_i kT$ tends to $3 \ln \Lambda - 1 - 1.49602$, whereas for $\Lambda \gg 1$ it tends to 0.76758Λ , and therefore set

$$\left(\frac{F_{\text{OCP}}}{\sum N_i kT}\right)_{\text{liq}} = \frac{F_{\text{vib}}}{\sum N_i kT} + 1.49602 - 0.32351 - 1.5 \ln \Gamma - H_l(\Gamma). \quad (39)$$

The OCP free energies include the contribution of the translational degrees of freedom. Since our free energy already includes $\sum F(T, V, N_i)$, we must, in order to obtain F_{CQ} , *subtract*

F^0 from each one of the F_{OCP} 's. Thus, finally,

$$\begin{aligned} \left(\frac{F_{CQ}}{\sum N_i kT} \right)_{liq} &= \frac{F_{\text{vib}}}{\sum N_i kT} - 3 \ln \Lambda + 2.49602 - H_l(\Gamma), \\ \left(\frac{F_{CQ}}{\sum N_i kT} \right)_{sol} &= \frac{F_{\text{vib}}}{\sum N_i kT} - 3 \ln \Lambda + 1.32351 + 1.5 \ln \Gamma - H_s(\Gamma). \end{aligned} \quad (40)$$

Formally, the difference between the liquid and solid free energies leads to a phase transition when

$$1.49602 - H_l(\Gamma) = 0.32351 + 1.5 \ln \Gamma - H_s(\Gamma). \quad (41)$$

The root of this equation, the ‘melting Γ ’, is $\Gamma_m = 178.2119$. We avoid this complication by interpolating for F_{CQ} in the interval $(\Gamma_m - 2, \Gamma_m + 2)$.

We shall not pause to write down the equations—such as $\mu_{\text{H}_2} = 2\mu_{\text{H}}$ for $\text{H}_2 \leftrightarrow 2\text{H}$, or $\mu_{\text{He}} = \mu_{\text{He}^+} + \mu - mc^2$ for $\text{He} \leftrightarrow \text{He}^+ + e$ —that determine the various states of hydrogen or helium (e.g. Pols et al. (1995)).

3.2 Opacities

The opacities, which generally depend on density, temperature and composition, are of two kinds: radiative and conductive. For the radiative part we use Boothroyd’s interpolation program¹ to interpolate within the OPAL Rosseland mean opacity tables (Iglesias & Rogers 1996). Each one of the OPAL tables is for a given hydrogen mass fraction X , a given total heavy element mass fraction Z (distributed in accordance with one of a number of standard ‘mixes’), a given carbon mass fraction excess X_C (such that the total carbon mass fraction is X_C , plus the carbon mass fraction contained in Z), and a given oxygen mass fraction excess X_O . The helium mass fraction is of course $1 - X - Z - X_C - X_O$.

Each one of the OPAL tables spans a temperature range $3.75 < \log T < 8.70$ and a range $-8 < \log R < +1$ of $\log R$ values, where $R = \rho/T_6^3$, with a cutout at the high T , high R corner, and sometimes at the low T , low R , corner. Boothroyd’s interpolation program provides the OPAL opacity κ , together with its density and temperature derivatives. (In this section, T is in degrees Kelvin, ρ in gr cm^{-3} , and κ in $\text{cm}^2 \text{g}^{-1}$.)

At the low temperature end the OPAL opacities are supplemented by the Ferguson et al. (2005) tables. These span a temperature range $2.70 < \log T < 4.50$, and the same R range as the OPAL tables. But their Z range has the upper limit $Z = 0.10$, and there is no

¹ Website <http://www.cita.utoronto.ca/~boothroy/kappa.html> .

provision for C or O excesses. We interpolate among them with a Z value equal to the lesser of $Z + X_C + X_O$ and 0.1.

At the high temperature end, $\log T > 8.70$, we extend the OPAL opacities by using electron/positron scattering opacity according to the fit of Iben (1975):

$$\kappa_{es} = [0.2 - D - (D^2 + 0.0004)^{1/2}]2n_{ep}/(N_A\rho), \quad D = 0.05(\log T_6 - 1.7), \quad (42)$$

where n_{ep} is the *sum* of the electron and positron number densities.

Electronic conductivities are taken from the Cassisi et al. (2007) tables. These span the temperature range $3 < \log T < 9$ K, and the density range $-6 < \log \rho < 9.75$. There is one such table for each value of the atomic number Z_{ion} , in fact 15 tables spanning the range $1 < Z_{ion} < 60$. We use the interpolation program provided by Cassisi et al. (2007), with Z_{ion} equal to the square root of the average (by number) squared atomic number

$$\left(\sum Z_i^2 X_i/A_i\right)/\left(\sum X_i/A_i\right).$$

The conductivity is converted to a conductive opacity and—harmonically—combined with the radiative opacity.

The various opacity interpolation programs provide the opacity κ , together with its density and temperature derivatives. But an evolution code that simultaneously solves for the stellar structure *and* composition requires the derivatives of κ with respect to composition as well. One way to get these is to evaluate the opacity at neighbouring compositions and then form difference ratios.

Alternatively, we use the following method, which yields continuous opacity derivatives: at the beginning of the evolutionary run, we use the various interpolation programs to create a set of total—radiative and conductive—opacity tables that, for the initial stellar model's Z , span the triangular region of Fig. 1. Along the x -axis of this figure we have seven values of the hydrogen mass fraction X , from 0 to $1 - Z$, *with no carbon or oxygen mass excesses*. Along the y -axis there are seven values of the *combined* C/O excess $X_{CO} = X_C + X_O$, again from 0 to $1 - Z$. Each point with positive X_{CO} corresponds to a pair of tables: one with carbon excess equal X_{CO} and zero oxygen excess (that is, 'excess all carbon'), and the other one with the same total excess X_{CO} , but 'excess all oxygen'. The $X_{CO} > 0$ tables have the lower limit $\log T = 4.00$, because the low-temperature Ferguson-Alexander tables correspond to zero C/O excesses.

There are no points to the right of the hypotenuse (because they would correspond to negative helium mass fraction $1 - Z - X - X_{CO}$). Our total number of opacity tables is 49,

and these replace the much larger number of OPAL, Ferguson-Alexander, and Cassisi tables. During MS hydrogen burning, the stellar core follows a path—from right to left—along the x -axis. During the HB (Horizontal Branch, core helium burning), C/O excesses rise and the core follows an upward path along the y -axis. Convective mixing may require the evaluation of the opacity in material containing both hydrogen and C/O excesses, that is, at points inside the triangle of Fig. 1.

In interpolating within the set of tables represented in Fig. 1, we distinguish between three cases:

Case I—No CO excesses. Interpolation is performed only within the 7 x -axis (hydrogen) tables. Within each table we use cubic Hermite splines to interpolate in $\log R$ and $\log T$, in order to obtain $\log \kappa$ and its T and R derivatives. Among the seven resulting values of $\log \kappa$, we then interpolate in order to obtain the final opacity value, together with its X derivative, for the required hydrogen mass fraction. Similar interpolations among the seven T derivatives, and among the seven R derivatives, yield the T and R derivatives for the required X . (Since $R = \rho/T_6^3$, the ρ derivative is simply related to the T and R derivatives.)

Case II—no hydrogen—interpolation within y -axis tables (where for each X_{CO} value there are two tables, the excess being completely in C for one, and completely in O for the second). We begin as in case I, by interpolating first among the ‘excess all carbon’ tables, and then among the ‘excess all oxygen’ tables. The final value of $\log \kappa$ is then obtained by linear interpolation:

$$\log \kappa = \frac{X_C}{X_{CO}} \log \kappa_C + \frac{X_O}{X_{CO}} \log \kappa_O, \quad (43)$$

$\log \kappa_C$, $\log \kappa_O$ denoting the opacities as obtained separately from tables for which excesses are all in C and from tables for which excesses are all in O, respectively. Composition derivatives of the opacity, with respect to X_C , or with respect to X_O , are then obtained from the last formula. The final T and R derivatives are obtained by similar, linear interpolations.

In comparing $\log \kappa$ obtained by this method with the one returned by Boothroyd’s interpolation (which has its own uncertainties), we found deviations of no more than a few percent. And the largest of these were at fairly low temperatures, $\sim 5.5 \lesssim \log T \lesssim 6.5$, where CO-rich opacities are less likely to be needed.

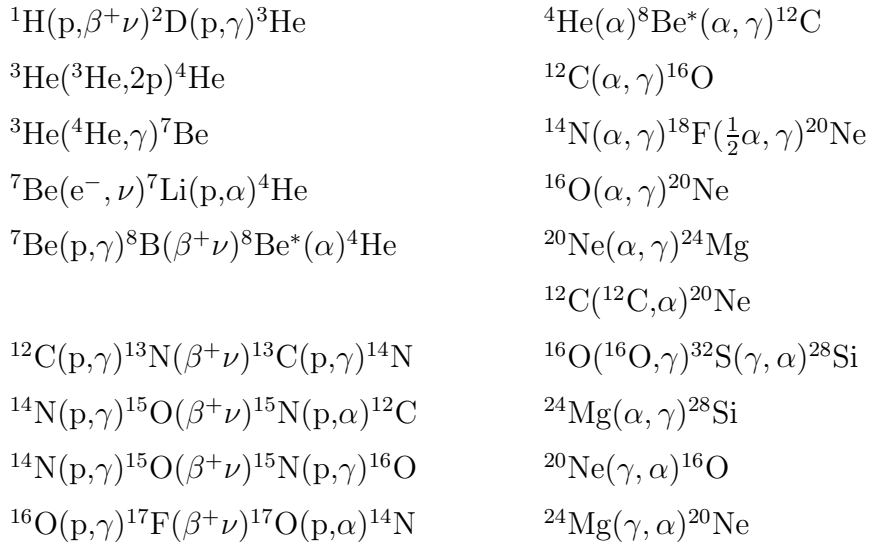
Case III—both C/O excess and hydrogen—interpolations inside the triangle of Fig. 1. This is a combination of Cases I and II.

In Fig. 2 we display opacity profiles, alongside temperature, density and composition

profiles, at three snapshots during a solar model evolution (§4.1)—Mid-MS, tip of RGB and the end-state as a cooling WD. Note that ranges of the y-axes values differ in between the three snapshots (columns), and it is apparent that there is a general decrease in opacity with the advance of evolution. The peak of opacity at low temperatures (around a few 10^4 K), close to the surface, is due to the ionization of hydrogen.

3.3 Nuclear Reaction Rates

We use the following nuclear reaction network:



with rates taken from Caughlan & Fowler (1988)². The enhancement of the nuclear reactions by electron screening is taken into account by following the prescriptions of Graboske et al. (1973).

Where several reactions are written in a chain, the later reactions are taken to be in transient equilibrium with the first one. The first five reactions—which constitute the pp-chain—are also assumed to be in transient equilibrium with each other, so that only the two major isotopes, ${}^1\text{H}$ and ${}^4\text{He}$, need to be followed. Similarly, in the next four reaction chains—which constitute the CNO cycle—only the major isotopes ${}^{12}\text{C}$, ${}^{14}\text{N}$, and ${}^{16}\text{O}$ are followed, and all other isotopes are taken to be in transient equilibrium.

The triple-alpha reaction ${}^4\text{He}(\alpha) {}^8\text{Be}^*(\alpha, \gamma) {}^{12}\text{C}$, together with the four following lines, constitute helium burning, which involves two further major isotopes— ${}^{20}\text{Ne}$ and ${}^{24}\text{Mg}$. The

² Website <http://www.phy.ornl.gov/astrophysics/data/cf88/> .

reaction $^{18}\text{F}(\frac{1}{2}\alpha, \gamma)^{20}\text{Ne}$ is of course a fiction (Pols et al. 1995), intended to avoid the creation of ^{22}Ne , which is thus replaced by ^{20}Ne .

Carbon burning proceeds—with comparable probabilities—through the two main branches $^{12}\text{C}(\text{C}, \text{p})^{23}\text{Na}$, $^{12}\text{C}(\text{C}, \alpha)^{20}\text{Ne}$. Since the protons released by the first one interact with other species, in particular through the reaction $^{23}\text{Na}(\text{p}, \alpha)^{20}\text{Ne}$, the net result of carbon burning can be described by the single reaction $^{12}\text{C}(\text{C}, \alpha)^{20}\text{Ne}$ (Iliadis 2007).

Oxygen burning proceeds via many branches: the main product is ^{28}Si , with ^{32}S a close second (*ibid.*). We take ^{28}Si as our last major isotope. Thus, after oxygen burning, our ^{28}Si mass fraction is actually the sum of $X(^{28}\text{Si})$ and $X(^{32}\text{S})$.

Carbon burning $^{12}\text{C}(\text{C}, \alpha)^{20}\text{Ne}$, neon photodisintegration $^{20}\text{Ne}(\gamma, \alpha)^{16}\text{O}$, and oxygen burning $^{16}\text{O}(\text{O}, \gamma)^{32}\text{S}(\gamma, \alpha)^{28}\text{Si}$, all release α particles that can be captured by ^{16}O , ^{20}Ne , or ^{24}Mg through the reactions listed above.

In accordance with the foregoing remarks, we need only follow changes in eight active isotopes, namely ^1H , ^4He , ^{12}C , ^{14}N , ^{16}O , ^{20}Ne , ^{24}Mg , and ^{28}Si . Thus, in eqs. (5)–(6), or in eqs. (9e)–(9f), the index j runs over the active isotopes, from 1 to 8. [The number of active isotopes may be changed, provided that the nuclear reaction network is modified accordingly.] Other isotopes, such as ^{40}Ca or ^{56}Fe , are regarded as inert: they contribute to the EOS, but their abundances do not change; in particular, they do not undergo convective mixing. For consistency, then, their abundances should be uniform throughout the initial stellar configuration, and so they will remain.

3.4 Neutrino Losses

Neutrino losses are according to Itoh et al. (1996), accounting for neutrino formation processes of pair annihilation, photo annihilation, plasma decay, bremsstrahlung and (optionally) recombination. There is also an option for using the older fitting formulae of Beaudet et al. (1967).

3.5 Convection (diffusive-convective mixing)

So long as the radiative ‘temperature gradient’ $d \ln T / d \ln p$, defined by

$$\nabla_{\text{R}} = \frac{\kappa L}{4\pi c G m} \frac{p}{4p_{\text{R}}}, \quad (44)$$

does not exceed the adiabatic

$$\nabla_{\text{A}} = \frac{\partial \ln T(p, s, X)}{\partial \ln p}, \quad (45)$$

the actual gradient ∇ , which appears in eq. (9c), is equal to ∇_{R} , and the diffusion coefficients σ_j in eq. (9e) are all zero: there is neither convective heat transport, nor any convective mixing. We hope that the specific entropy s in (45) will not be confused with $s = r^2$.

Convection is taken to set in whenever

$$\Delta\nabla = \nabla_{\text{R}} - \nabla_{\text{A}} > 0. \quad (46)$$

The actual gradient ∇ is then calculated in accordance with the mixing length recipe (Mihalas 1978): consider the non-dimensional (inverse) convective efficiency parameter

$$b = \frac{16\sqrt{2}\sigma_{\text{R}}T^4}{(\ell/H)\sqrt{Q}\rho c_{\text{P}}T v_0\tau_e}, \quad (47)$$

where σ_{R} is Stefan's constant; ℓ is the mixing length, which we take to be a constant multiple (of order unity) of the pressure scale height $H = v_0^2/g$, where $v_0^2 = p/\rho$ is the squared thermal speed and $g = Gm/r^2$ is the local acceleration of gravity; $Q = -\partial \ln \rho(p, T, X)/\partial \ln T$; c_{P} is the specific heat at constant pressure; and $\tau_e = \kappa\rho\ell$. Let x be the root of the cubic equation

$$\frac{3}{4b'}x^3 + x^2 + 2b'x = 1, \quad (48)$$

where

$$b' = b/\sqrt{\Delta\nabla}, \quad (49)$$

Then the actual gradient is given by

$$\nabla = \nabla_{\text{A}} + (x^2 + 2b'x)\Delta\nabla. \quad (50)$$

It is readily seen that $\nabla \rightarrow \nabla_{\text{A}}$ as $b' \rightarrow 0$, and $\nabla \rightarrow \nabla_{\text{R}}$ as $b' \rightarrow \infty$.

Convective mixing is taken to be due to diffusion in a gas of particles—representing the convective elements—moving at the convective speed

$$v_c = \frac{\ell}{H} \left[\frac{Q}{8} \Delta\nabla \right]^{1/2} x v_0 \quad (51)$$

(Mihalas 1978), with the mean free path ℓ . In such a gas the diffusion coefficient is $\sim v_c\ell$.

But in eqs. (9e)–(9f) the derivatives are with respect to mass, not radius. We therefore set the convective diffusion coefficients equal to

$$\sigma_j = \left(\frac{dm}{dr} \right)^2 v_c \ell = (4\pi r^2 \rho)^2 v_c \ell, \quad (52)$$

the same for all species j .

The code sometimes runs into difficulties with the foregoing convective diffusion coefficients. We therefore retain an option whereby the last formula is replaced by a much simpler one:

$$\sigma_j = k_c \left(\frac{\Delta\nabla}{\nabla_{\text{R}}} \right)^2, \quad (53)$$

where $k_c < 1$ is a numerical coefficient. Its purpose is to ensure that convective mixing does not occur too suddenly. The value of k_c is related to the evolutionary time scale, and ranges from ~ 0.1 for low-mass stars to ~ 0.001 for massive ones.

Finally, the code has an option for introducing convective overshoot. This is done in a rather schematic way: at each iteration, after determining the convective zones in accordance with the inequality $\Delta\nabla > 0$, we repeat the determination of the zone boundaries, this time with $\Delta\nabla = \nabla_R - \nabla_A + \nabla_{OS} > 0$, where ∇_{OS} is a small, positive constant. The temperature gradient ∇ and the convective diffusion coefficient are then determined by the foregoing formulae, but with the new, augmented, $\Delta\nabla$. We do not attempt to fix ∇_{OS} by any dependence on local conditions (Pols et al. 1995).

3.6 Mass Loss

The stellar mass may change with time at a prescribed rate \dot{M} , according to boundary condition (18). This rate is generally taken to be a function of the stellar parameters $M_\star, L_\star, R_\star$. Over the years, several formulae have been suggested in the literature, each fitting observations of stars in a particular evolutionary phase. We mention them briefly below, with the mass loss rate (MLR) in units of $M_\odot \text{ yr}^{-1}$.

1. The earliest such expression is Reimers's formula (Reimers 1975), derived from observations of RGB stars,

$$\dot{M}_{\text{Reim}} = -4 \times 10^{-13} \eta_{\text{Reim}} \frac{L_\star R_\star}{M_\star}, \quad (54)$$

where the coefficient η_{Reim} lies between 0.3 and 3.0.

2. A fit for early type O and B stars, with somewhat modified powers of $M_\star, L_\star, R_\star$, is given by Lamers (1981):

$$\dot{M}_{\text{Lam}} = -10^{-4.83} \left(\frac{L_\star}{10^3}\right)^{1.42} \left(\frac{R_\star}{30}\right)^{0.61} \left(\frac{M_\star}{30}\right)^{-0.99}. \quad (55)$$

3. A modification of Reimers's MLR, allowing for a superwind on the AGB, is given by Baud & Habing (1983):

$$\dot{M}_{\text{BH}} = \dot{M}_{\text{Reim}} \times \frac{M_{\text{env},0}}{M_{\text{env}}}, \quad (56)$$

where $M_{\text{env},0}$ is the envelope mass at the base of the AGB.

4. Another variation on Reimers's MLR, similar to \dot{M}_{Lam} , is given by Nieuwenhuijzen & de Jager (1990) (subsequent paper to de Jager et al. 1988, where \dot{M} was given as a function of T_{eff}, L):

$$\dot{M}_{\text{NDJ}} = -9.63 \times 10^{-15} L_\star^{1.42} R_\star^{0.81} M_\star^{0.16}. \quad (57)$$

5. The strong increase in mass-loss rate during the AGB stage is rendered by the MLR formulae of Bloeker (1995), which are based on an investigation of long period variables and shock-driven winds by Bowen (1988). Bloeker’s MLR formula is:

$$\dot{M}_{B1} = 4.83 \times 10^{-9} \dot{M}_{Rei} M_{ZAMS}^{-2.1} L_{\star}^{2.7}, \quad (58)$$

and a variant, \dot{M}_{B2} , has M_{ZAMS} replaced by M_{\star} .

6. Yet another modification of Reimers’s formula, intended for cool winds that are not driven by molecules or dust, is given by Schröder & Cuntz (2005), Schröder & Cuntz (2007):

$$\dot{M}_{SC} = -\eta_{SC} \frac{L_{\star} R_{\star}}{M_{\star}} \left(\frac{T_{eff}}{4000K} \right)^{3.5} \left(1 + \frac{g_{\odot}}{4300g_{\star}} \right), \quad (59)$$

with $\eta_{SC} = 8(\pm 1) \times 10^{-14}$. Here two new factors are included, taking into account the dependence of chromospheric height on surface gravity and the dependence of the mechanical energy flux on the effective temperature.

In applying any of the MLR expressions, instead of turning it on suddenly, we multiply it by a Fermi weight function

$$F(R_{\star}) = \frac{1}{1 + e^{(R_{thresh} - R_{\star})/(0.05R_{thresh})}}, \quad (60)$$

where R_{thresh} is an MLR threshold radius, which we typically choose between 1 and 50. Its precise value is not important, so long as the MLR is negligible for $R = R_{thresh}$. As R_{\star} increases, $F(R_{\star})$ varies smoothly near R_{thresh} from 0 to 1, over a width of $0.05R_{thresh}$. This prevents an on-off situation, which can ruin the convergence of the iteration process by which the difference equations of §2.2 are solved.

The question remains, which formula to use? The code includes an algorithm that identifies the evolutionary stage of the stellar model by testing various parameters (such as luminosity, radius, composition profiles) and their rates of change. Therefore, one may pass — in a smooth manner — from one formula to another. In this work, we used (54) for the RGB and (58) for later stages. The parameter η_{Reim} was taken progressively higher with increasing initial mass. The effect of R_{thresh} and η_{Reim} on the results will be briefly discussed in section §4.4.

4 EVOLUTION SEQUENCES

Using the evolution code described in the previous section, we performed calculations over a wide range of initial stellar masses and metallicities. In the following sections we address representative results, outcome of continuous calculations that yield complete evolutionary

tracks, starting from an initial pre-main-sequence state and ending with either a cooling white dwarf (for initial masses below $9 M_{\odot}$), or core collapse of a configuration resembling a supernova progenitor (for higher initial masses). We use the following acronyms: MS - main sequence; ZAMS - zero-age main sequence; pre-MS - pre-main-sequence; RGB - red giant branch; HeF - helium flash; HB - horizontal branch; AGB - asymptotic giant branch; TP - thermal pulse; WD - white dwarf; HRD - Hertzsprung-Russell diagram. Central properties are denoted by subscript c .

4.1 Solar Model

We started from a 'pre-MS' configuration of $1 M_{\odot}$, of uniform composition $Y = 0.29$ and $Z = 0.018$ —the latter with a heavy element distribution according to Grevesse & Noels (1993)—and a radius of $2.7 R_{\odot}$. With a mixing-length to scaleheight ratio $\alpha \equiv l/H_P = 2.5$, this configuration reached the ZAMS after 0.05 Gyr. At an age of 4.60 Gyr—which includes the 0.05 Gyr from pre-MS to ZAMS—the model reached a radius of $1.006 R_{\odot}$, a luminosity of $1.009 L_{\odot}$, and central characteristics $T_c = 15.59 \times 10^6$ K, $p_c = 2.453 \times 10^{17}$ dyn cm $^{-2}$, $\rho_c = 157.9$ gr cm $^{-3}$. We regard this as a good match to the present sun, and the central characteristics in agreement with those obtained by other codes (e.g., Reiter et al. 1995, Turcotte et al. 1998, Morel et al. 2000). It should, perhaps, be noted that our mixing-length recipe uses the constants of Mihalas (1978), and our choice of $\alpha = 2.5$ may correspond to different values for other choices of the constants.

Fig. 3 shows the evolutionary track in the HRD, where the various phases are marked: from pre-MS, through MS, RGB and core HeF, settling into stable core He burning, continuing through AGB and thermal pulses up to the last He shell flashes—where a strong flash occurs, followed by a weaker one—and ending with a cooling $0.55 M_{\odot}$ CO-WD. The durations of the MS, RGB and HB stages are 10 Gyr, 1.5 Gyr and 78 Myr, respectively. The maximum radius and luminosity—attained on the AGB after some 11.7 Gyr of evolution (from ZAMS)—are $1.46 \times 10^2 R_{\odot}$ and $2.81 \times 10^3 L_{\odot}$, respectively. The maximum temperature throughout the evolution, 2.09×10^8 K, is attained off-center, at the tip of the AGB. We terminated the calculation with a final CO-WD of radius $R_{WD} = 2.13 \times 10^{-2} R_{\odot}$, a central pressure $p_{c,WD} = 6.94 \times 10^{22}$ dyn cm $^{-2}$, a central density $\rho_{c,WD} = 1.84 \times 10^6$ gr cm $^{-3}$ and a core temperature of ~ 75 million K.

4.2 The Effect of Metallicity

The effect of metallicity on stellar evolution is illustrated by a series of calculations for a model of solar mass and (Z, Y) values of $(0.0001, 0.24)$, $(0.001, 0.24)$, $(0.018, 0.29)$, $(0.05, 0.30)$ and $(0.1, 0.30)$, other physical and numerical parameters remaining fixed. The results are presented in Fig. 4 by complete, continuous tracks in the H-R diagram. We note that an increase in metallicity has a similar effect to a decrease in the initial stellar mass: luminosities are lower and the durations of evolutionary phases are longer. For example, the MS phase lasts up to over 3 times longer, when Z increases from 10^{-4} to 0.1. This result is mostly the consequence of the dependence of opacity on composition; at a lower metallicity, the opacity decreases, the star is able to radiate away its energy with greater efficiency, the stellar luminosity is therefore higher and timescales are correspondingly shorter.

Apart from the apparent shift of the evolutionary tracks in the H-R diagram, and the different timescales, metallicity also affects the final masses. For $M_i = 1 M_\odot$, a final mass of $0.57 M_\odot$ was obtained for the lowest metallicity ($Z = 0.0001$), and $0.52 M_\odot$ for the highest one ($Z = 0.1$), as compared with $0.55 M_\odot$, obtained for solar metallicity—an overall spread of almost 10%.

4.3 Canonical Evolution Sequences

We consider Population I (Pop.I) and Population II (Pop.II) stars, adopting metallicities of $Z = 0.01$ and $Z = 0.001$, respectively, and initial masses in the range $0.25 - 9 M_\odot$, leading to cooling WDs. The complete evolutionary tracks are shown in the two panels of Fig. 5. Timescales and the final WD masses and composition are given in the accompanying Table 1. It should be noted that the MS and RGB durations as shown in the table depend on the definition of the MS-turnoff point and beginning of the RGB, which involves some arbitrariness. The criterion we use for the MS turnoff is as follows: let t_1 be the time when X_c has decreased below 10^{-6} ; let $x_1 = \log T_{eff}(t_1)$ and $y_1 = \log L(t_1)$. The turnoff time t_2 is the earliest time for which the distance between the points $[x_2 = \log T_{eff}(t_2), y_2 = \log L(t_2)]$ and $[x_1, y_1]$ in the $[\log T_{eff}, \log L]$ plane exceeds 0.1. Similar criteria are used for other transitions between evolutionary stages. Time scales depend strongly on composition, especially on Z , decreasing with decreasing Z . Given differences in composition adopted in different studies, as well as differences in criteria defining evolutionary stages, a precise comparison between models is difficult to achieve. Nevertheless, we find excellent agreement, for example, between

our low-mass Pop.II models and corresponding ones calculated by others: for the $0.8 M_{\odot}$ and $1 M_{\odot}$ models, we find $\tau_{MS} = 1.44 \times 10^{10}$ yr and 6.02×10^9 yr, respectively (see Table 1), while for the same masses and metallicity, Charbonnel et al. (1996) find 1.51×10^{10} yr and 6.06×10^9 yr, and Charbonnel et al. (1999), after modifying the input physics, find 1.43×10^{10} yr and 6.85×10^9 yr. For Pop.I models, the spread in initial Z is larger, yet our results are compatible with those obtained by Serenelli & Fukugita (2007) for a grid of stellar models with $Z = 0.019$.

The evolutionary tracks end with a cooling WD. A He-WD is obtained for the lower initial masses, $0.25 \lesssim M_i \lesssim 0.50 M_{\odot}$. The transition to a CO-WD occurs between 0.50 and $0.80 M_{\odot}$, and the heavier ONeMg-dominated WDs are obtained for initial masses higher than $\sim 8 M_{\odot}$ (the transition mass being higher for the Pop.I stars). It should be noted, however, that especially for the Pop.I stars, the transition mass for obtaining a CO-WD rather than a He-WD is strongly dependent on the mass-loss rate assumed. For example, for an initial mass of $0.80 M_{\odot}$, slightly increasing the mass-loss rate may result either in a He-WD, when the threshold for core helium burning is not reached, or, in an Extreme Horizontal Branch (EHB) star, when a ‘delayed’ core HeF takes place. The production of such hot (blue) HB stars for relatively low initial masses (from around 0.80 to slightly over $1 M_{\odot}$) and for a range of metallicities will be addressed in a subsequent paper.

For both populations, a violent ignition of helium takes place in the core (but usually off-center, because of neutrino cooling) at the tip of the first giant branch for masses in the range $0.80 - 2 M_{\odot}$. This is the well-known core HeF. The transition between HeF and quiet He ignition occurs at an initial mass between 2 and $3 M_{\odot}$, depending mainly on composition and mass-loss rate. During the flash, the peak nuclear energy generation rate is in the range $5 \times 10^7 \lesssim L_{nuc,max} \lesssim 5 \times 10^9 L_{\odot}$, decreasing with increasing initial mass, due to a corresponding decrease in the degree of electron degeneracy of the core material. It is worth noting that the luminosity of the star during the flash is unaffected by what is taking place in the core, despite the huge nuclear luminosity, which surpasses the luminosity obtained at any evolutionary stage. The overall duration of the flash (when L_{nuc} is in excess of, say, $10^5 L_{\odot}$) is of the order of a few years. We note that during this stage time steps are automatically reduced down to days, then hours and minutes. Once the flash is over, it will take some extra 10^3 to 10^5 years before the star settles into stable core He burning, the HB phase.

The well-known thermal pulses that arise as a result of the double shell-burning instabil-

ity, are clearly seen in the evolutionary sequences during the final stages of the AGB. Fig. 6 shows a typical example for a Pop.II, $2 M_{\odot}$ model. The thermal pulses in this example span about 7×10^5 yr, and clear trends are evident, such as the monotonic decrease in effective temperatures with advancing pulses, along with an increase in the radial extension of the photosphere, which reflect the asymptotic evolution towards the redder tip of the AGB. Also evident is the fact that the bulk of mass-loss takes place precisely during this short phase, with the mass dropping from 1.90 to $0.63 M_{\odot}$ - almost its final value. The mass of the H-depleted core increases during this phase from 0.58 to $0.62 M_{\odot}$; the mass of the inner He-depleted core increases from 0.48 to $0.54 M_{\odot}$. Since the He profile is not as steep as the H profile, the mass of the He-depleted core is a matter of definition: here 'He-depleted' means $Y < 10^{-6}$. Taking the core boundary at the mid-point of the He profile yields a final He-depleted core mass of $0.60 M_{\odot}$. We should note that the total number of pulses in each evolutionary sequence is largely determined by the mass-loss law adopted.

4.4 Mass-Loss Laws and Initial-Final Mass Relationship (IFMR)

Using the complete evolutionary tracks for the mass range of 0.8 to $9 M_{\odot}$, for both populations $Z = 0.01$ and $Z = 0.001$, as listed in Table 1, we obtain a theoretical IFMR, displayed in Fig. 7 (solid and dashed black lines). We increased the number of points by adding results for masses of 2.5 and $3.5 M_{\odot}$, and for $Z = 0.02$ and $Z = 0.005$ and masses of $1, 3$ and $5 M_{\odot}$ (marked in Fig. 7 by different symbols). Similar relationships have been recently computed by Meng et al. (2007) and by Catalán et al. (2008), the latter including earlier results obtained by Dominguez et al. (1999). A different and independent source for such a relationship is provided by observations (e.g., Weidemann 2000), mainly of star clusters, which lead to empirical or semi-empirical linear relations, such as Ferrario et al. (2005) (based on open-cluster data for the range $2.5 - 6.5 M_{\odot}$) and others that will be mentioned below.

The curves obtained here show that the IFMR may be divided into three regions with different slopes: 1. A moderate slope for $M_i \lesssim 3 M_{\odot}$, which coincides with the tabulated results of Weidemann (2000) plotted in Fig. 7. 2. A steeper slope for $3 \lesssim M_i \lesssim 4 M_{\odot}$. 3. Again, a more gradual increase until the top end. We note that the 'new relation' as displayed in Fig. 2 of Herwig (1995), meant to fit only the best determined stars of the Hyades and Pleiades clusters, has a very similar shape to our curves, only shifted upwards from our Pop.I curve by about $0.05 M_{\odot}$.

The dependence on metallicity is apparent from the divergence of the two curves in Fig. 7, in agreement with the conclusions of e.g. Meng et al. (2007) or the Dominguez et al. (1999) curves as plotted in Fig. 5 of Catalán et al. (2008). The effect of metallicity is negligible for $M_i \lesssim 2 M_\odot$ (in agreement with e.g. Catalán et al. (2008)), but it increases towards higher initial masses: the curves diverge by $\gtrsim 0.13 M_\odot$ at the top end $M_i \gtrsim 7 M_\odot$. Meng et al. 2007 reach a difference of up to $0.4 M_\odot$ in the final masses derived from different metallicities, their study covering a broad metallicity range: Z in between 0.0001 and 0.1. They also notice a minimum of the IFMR for $Z = 0.04$.

Various semi-empirical linear fits have been derived over the last decade. A few examples are:

Ferrario et al. (2005) (based on open-cluster data for the range $2.5 - 6.5 M_\odot$; claiming that the IFMR can be modelled by a mean relationship about which there exists some intrinsic scatter, and that they ‘cannot justify the use of any but a linear relationship to model the cluster data’):

$$M_f = (0.10038 \pm 0.00518)M_i + 0.43443 \pm 0.01467 \quad (61)$$

Dobbie et al. (2006) (a linear fit to some 27 WDs, members of clusters such as the Hyades, Praesepe, M35, NGC2516 and the Pleiades, over initial-mass range of $2.7 - 6 M_\odot$):

$$M_f = (0.133 \pm 0.015)M_i + 0.289 \pm 0.051 \quad (62)$$

Williams (2007) (claiming that the IFMR is both linear and without any metallicity dependence):

$$M_f = (0.132 \pm 0.017)M_i + 0.33 \pm 0.07 \quad (63)$$

Although the relations obtained, as shown in Fig. 7, are quite far from linear, the closest linear fit that we can suggest, without using any artificial anchoring, is

$$M_f = 0.08343 * M_i + 0.47321 \quad (64)$$

which falls slightly above the upper (Pop.II) curve around the lower initial masses ($1.5 - 2.5 M_\odot$), and below the lower (Pop.I) curve for higher intermediate masses, around $5 M_\odot$. This fit is very similar to the linear fit of Ferrario et al. (2005) (shown in Fig. 7), although the latter is limited to the range 2.5 to $6.5 M_\odot$.

Clearly, the relation obtained represents the set of parameters assumed, mostly those related to the mass-loss recipe. The value of η_{Reim} used here was linearly increased from 0.4 at $0.8 M_\odot$ to 3.0 at $9 M_\odot$. A preliminary comparison that we performed, keeping all parameters

fixed and changing only mass-loss laws, indeed showed some differences in the final WD masses, with a spread of less than 10%. More precisely, for our solar model parameters (see §4.3), setting $\eta_{\text{Rei}} = 0.6$, $R_{\text{thresh}} = 50$, the derived final WD masses were all in the range $0.53 - 0.57 M_{\odot}$ (or between $0.51 - 0.56$ for slightly higher mass-loss rates obtained by using $\eta_{\text{Rei}} = 1.0$, $R_{\text{thresh}} = 10$). Performing the same comparison for $3 M_{\odot}$ ($Z = 0.01$), but using $\eta_{\text{Rei}} = 2.0$, we found final WD masses to be in the range $0.61 - 0.67 M_{\odot}$.

4.5 Massive Stars

We now briefly consider Pop.I massive stars of initial masses in the range $16 - 64 M_{\odot}$, typically, SN progenitors. Since nucleosynthesis calculations are limited in our code, we cannot follow the evolution all the way to the collapse of an iron core. However, we come quite close to it. These massive stars go through advanced nuclear burning stages, until a core composed of the end-product of our nuclear reactions network is obtained. Core masses range monotonically from $2.4 M_{\odot}$ for the $64 M_{\odot}$ initial mass and $1.7 M_{\odot}$ for the $16 M_{\odot}$ initial mass. The core is enveloped by layers of different composition, the outermost being predominantly helium. Envelope masses depend strongly on the mass loss law assumed.

The core contracts, becoming degenerate and unstable, since its mass exceeds the Chandrasekhar limit. As contraction accelerates, temperatures rise to a few 10^{10} K, where electron-positron pairs are created, which enhances the instability, lowering the adiabatic exponent. Pair production replaces iron photodisintegration as the mechanism leading to core collapse. Density profiles throughout the stars are shown in Fig. 8. The code crashes when the collapse approaches free-fall, with the adiabatic exponent very close to $4/3$ throughout the core. Since this point is somewhat arbitrary, the curves representing stars of different initial masses do not exhibit a perfectly regular (monotonic) behaviour; this is sometimes the case for evolutionary tracks or characteristics of massive stars in the late stages (Arnett 1996, Umeda & Nomoto 2008), resulting from the complexity of the processes taking part in them, and the related parameters and thresholds. We do not claim that these calculations shed light on pre-supernova evolution; rather, we mention them here as an example of the robustness of the code, which is capable of dealing with complex processes under critical conditions without failing.

Finally, adding the results obtained for lower masses of Pop.I, described in Section 4.3, we show in Fig. 9 evolutionary tracks of the stellar central points in the $(\log T, \log \rho)$ plane,

exhibiting the branching off between stars that end their lives as WDs, and stars that go through advanced nuclear burning stages, ending their lives in dynamic core collapse.

4.6 Non-Canonical Evolution

The term ‘non-canonical’ refers to stars of unusual internal structure and composition. Such configurations may result from stellar mergers, where the merging stars may be MS stars, giants, compact stars or any combination of different types. Stellar mergers are probably the progenitors of blue straggler stars (BSS), found to exist in environments of high stellar density, such as globular clusters or the cores of open clusters.

As already mentioned, the main reason for developing the evolution code presented here was the need for an efficient and fast tool that could be integrated into the MODEST (Modelling DENSE STellar systems) collaboration, combining dynamical N-body calculations with hydrodynamics—the colliding or merging of stars—and stellar evolution, for the simulating of dense stellar environments. Whereas for normal stars, it is possible to construct and tabulate pre-computed evolutionary tracks for the use of MODEST calculations, merger products, having completely unpredictable configurations, must be evolved *in situ*.

A non-canonical initial model will be the product of a hydrodynamic merger calculation, usually by smoothed particle hydrodynamics (SPH) methods. The first step in adapting such a model to quasi-static stellar evolution calculations is to obtain a hydrostatically relaxed configuration. This is achieved by applying the quasi-dynamic method of Rakavy et al. (1967). Instead of eqs. (1)–(2), consider the equations

$$\frac{1}{\rho} = \frac{\partial}{\partial m} \frac{4\pi}{3} r^3, \quad (65)$$

$$\frac{\partial r}{\partial \tau} = -4\pi r^2 \frac{\partial p(\rho, s, Y)}{\partial m} - \frac{Gm}{r^2}, \quad (66)$$

where $r(m, \tau)$ is regarded as a function of the mass coordinate m and the quasi-time τ , and $p(\rho, s, Y)$ is determined by the EOS. The quasi-time has no physical meaning: its purpose is provide asymptotically (i.e. for $\tau \rightarrow \infty$) a hydrostatic solution. Equation (66) is called quasi-dynamic because the correct dynamic equation would have $\partial^2 r / \partial t^2$ —with t the true time—on its left-hand side.

Let the boundary conditions be $r = 0$ at the center, and $p = 0$ at the surface. For a given distribution of entropy $s(m)$, and of the number fractions, collectively denoted by

$Y(m)$, and an initial distribution of radii $r(m, 0)$, the foregoing equations are to be solved for $r(m, \tau)$ (and $\rho(m, \tau)$, and $p(m, \tau)$).

Since the entropy s and the composition Y are not varied, the (quasi) motion is adiabatic: $du = -pd(1/\rho)$. Multiplying (66) by $\partial r/\partial\tau$ and integrating over the mass of the star yields, after an integration by parts,

$$\int_0^M \left(\frac{\partial r}{\partial\tau}\right)^2 dm = -\frac{dE}{d\tau}, \quad (67)$$

where

$$E = \int_0^M \left(u - \frac{Gm}{r}\right) dm \quad (68)$$

is the total energy, internal and gravitational. Equation (67) shows that the energy decreases with quasi-time. If—for the given entropy and composition distributions—a minimum of E exists, the solution of eqs. (65)–(66) must lead to it, and the resulting structure, of stationary energy, will be hydrostatic. If, on the other hand, a minimum of E does not exist, the configuration is dynamically unstable: E will then decrease indefinitely.

Thus, the quasi-dynamic method either leads to a hydrostatic structure, or else detects dynamical instability. It can be applied to any initial density distribution, even a uniform one. With the EOS

$$p(\rho, s, Y) = K\rho^{1+\frac{1}{n}} \quad (69)$$

it can be used to construct a polytrope (dynamically unstable when $n \geq 3$), which may serve as an initial ‘fully convective’ protostellar model of uniform entropy and composition. Of course, ‘solution’ of (65)–(66) entails the replacement of the differential equations by implicit difference equations, which are then solved by an iterative process (Rakavy et al. 1967).

As preliminary examples, we evolved merger products for three pairs of Pop.II ($Z = 0.001$) low-mass parent stars. The parent stars were evolved by our code from some pre-MS initial configuration, to an age when the more massive star of each pair was almost at terminal MS age (TAMS), the less massive star of the pair being, of course, at an earlier stage on the MS. A pair of 0.85 and 0.60 M_\odot parent stars was evolved for 11 Gyr; a pair of 1.00 and 0.60 M_\odot for 6 Gyr; and finally, a pair of 1.40 and 0.60 M_\odot for 1.5 Gyr. To calculate structures of the merger products for the above pairs of parent stars, we used the MMAS (‘make me a star’, version 1.6) package of Lombardi et al. (2002), which produces 1D models that approximate results of detailed SPH calculations. We chose to perform head-on

collisions (zero periastron separation), so that effects of rotation were absent. Each resulting merger product was incorporated *as is* into our code, and upon obtaining a hydrostatically relaxed configuration by the ‘quasi-dynamic method’ as explained above, calculation of the evolution was initiated.

It might be worthwhile to note the difference between the way we treat the merger-product and the way the non-canonical evolution is initiated by Glebbeek et al. (2008), Glebbeek & Pols (2008). As explained in these papers, what the authors did was to start from a ZAMS model of the correct mass, evolve it until the central X_H equalled that of the merger product and then evolve it further with a fictitious energy production until its entropy profile equalled that of the merger product. This was done in steps, during which the composition was gradually adjusted to that of the merger product. This process resulted in a hydrostatic configuration that had the given mass and correct entropy and composition profiles. In contrast, what we did was to make use of the merger product exactly as obtained by the collision calculation and subject it to the quasi-dynamic method.

Table 4.6 lists some details of the colliding stars and the resulting mergers: t_{col} is the time of collision (age to which the parent stars were evolved); M_{merger} is the mass of the merger product (slightly less than the sum of parent star masses, because some mass was lost in the merger process); Y_c is the central He mass-fraction, τ_{MS} is the remaining MS lifetime of the merger-product, whereas $\tau_{MS,counter}$ is the MS duration of the canonical counterpart - a normal (‘canonical’) star of initial mass equal to that of the merger-product. The central He mass fraction generally depends on the stages to which the parent stars have been evolved - how close to TAMS was the more massive parent star, and correspondingly, how much hydrogen did the less massive star of the pair managed to burn during its limited MS evolution. It should be noted, for instance, that the MS duration of the $1.88 M_\odot$ merger-product exceeds that of the lower-mass $1.48 M_\odot$ merger-product; this is due to the greater amount of central hydrogen in the more massive merger-product.

Fig 10 shows evolutionary tracks on HRD of the three merger products (solid lines) ($0.85 + 0.60$, $1.00 + 0.60$, $1.40 + 0.60$ - top to bottom), while dashed lines represent evolutionary tracks of the canonical counterparts. The non-canonical models, possessing excess thermal energy right after the merging process, all begin by gravitational contraction before settling on the MS, where they spend the time required for burning the remaining central hydrogen. It is only during the MS and early-RGB phases that the non-canonical track differs from that of the canonical one. The non-canonical track is shifted slightly upwards (to

Table 1. Collisions of low-mass MS parent stars - characteristics of the parent stars and merger-products. Masses are in solar units; MS durations are in years.

M_1	M_2	t_{col} (Gyr)	M_{merger}	Y_c	τ_{MS}	$\tau_{MS,counter}$
0.85	0.60	11.0	1.34	0.96	3.75e8	2.05e9
1.00	0.60	6.0	1.48	0.98	2.84e8	1.43e9
1.40	0.60	1.5	1.88	0.88	2.91e8	6.10e8

higher luminosity); the shift is growing with increasing mass (as is clearly apparent in the blow-up panels on the right). Except for the insignificant differences in the shape of the last shell flash while traversing the HRD from the AGB tip to the cooling WD curve, the tracks almost exactly overlap from RGB onwards.

Fig. 11 shows, as an example, composition profiles of the $1.40 + 0.60 M_{\odot}$ merger, with comparison to the $1.88 M_{\odot}$ canonical counterpart at the point when the latter’s Y_c equals that of the initial state of the merger product. In the top panel the H and He profiles of the merger-product are plotted together with those of the 1.40 and 0.60 parent stars. Central hydrogen is almost completely depleted for the more massive parent star, which is very close to its TAMS; the low-mass parent star, at early stages of its MS evolution, still has a large fraction of hydrogen.

Already a decade ago Sills et al. (1997) began investigating evolutionary scenarios of collisionally merged stars, with the aim of examining possible formation channels and properties of blue straggler stars in globular clusters. They present results of evolutionary calculations for seven head-on collisions. Among their results, we find for instance a MS duration of 3.74×10^8 yr for their $0.80 + 0.60 M_{\odot}$ merger; although details of the collision, including abundances, might not be exactly comparable, this result seems to be in very good agreement with our derived MS duration of 3.75×10^8 yr for our $0.85 + 0.60 M_{\odot}$ similar merger.

As mentioned, more extensive evolutionary calculations for collision products have recently been performed by Glebbeek et al. (2008), Glebbeek & Pols (2008). Nowadays, several procedures for performing calculations of stellar collisions, such as the mentioned MMAS by Lombardi et al. (2002) or MMAMS (‘make me a massive star’) by Gaburov et al. (2008) are available. As illustrated by the foregoing three examples, our code is able to import and initiate evolution for merger-products created by either of the above procedures. In future, it will be interesting to study non-canonical evolution merger-products over a wider range of masses and initial compositions (outcomes of various combinations of the parent stars), as well as mergers involving other types of stars, such as compact objects—the merging of WD-MS or WD-WD.

SUMMARY

We have developed a stellar evolution code that is capable of calculating full evolutionary tracks without interruption or intervention. The implicit numerical scheme is based on simultaneous solution of the thermodynamic and composition equations on an adaptive grid. Time steps are self-adjusting according to numerical as well as evolutionary time-scale criteria. The code was applied to a large variety of examples: full evolutionary tracks for stars of a wide range of masses and metallicities, and non-canonical stars obtained from stellar mergers. We believe that these examples of stellar evolution calculations demonstrate the efficiency and robustness of our new code. We mention, in particular, the ability of the code to deal with the core He flash, thermal pulses, WD cooling, core collapse, as well as non-canonical configurations. We thus expect it to be useful in extensive parameter studies—of both stellar physics and initial properties of stellar models—as well as in simulations of stellar clusters.

ACKNOWLEDGMENTS

We are grateful to James Lombardi for providing us with his MMAS code. We also wish to thank Onno Pols for a very careful reading of the original manuscript and numerous comments and helpful suggestions. This work was supported in part by the Israel Science Foundation grant 388/07.

REFERENCES

- Aarseth S. J., 1963, *MNRAS*, 126, 223
- Aarseth S. J., 1999, *PASP*, 111, 1333
- Arnett D., 1996, *Supernovae and nucleosynthesis. an investigation of the history of matter, from the Big Bang to the present.* Princeton series in astrophysics, Princeton, NJ: Princeton University Press, —c1996
- Baud B., Habing H. J., 1983, *A&A*, 127, 73
- Beaudet G., Petrosian V., Salpeter E. E., 1967, *ApJ*, 150, 979
- Blöcker T., 1995, *A&A*, 297, 727
- Bowen G. H., 1988, *ApJ*, 329, 299
- Cassisi S., Potekhin A. Y., Pietrinferni A., Catelan M., Salaris M., 2007, *ApJ*, 661, 1094
- Catalán S., Isern J., García-Berro E., Ribas I., Allende Prieto C., Bonanos A. Z., 2008, *A&A*, 477, 213
- Caughlan G. R., Fowler W. A., 1988, *Atomic Data and Nuclear Data Tables*, 40, 283
- Charbonnel C., Däppen W., Schaerer D., Bernasconi P. A., Maeder A., Meynet G., Mowlavi N., 1999, *A&AS*, 135, 405
- Charbonnel C., Meynet G., Maeder A., Schaerer D., 1996, *A&AS*, 115, 339
- de Jager C., Nieuwenhuijzen H., van der Hucht K. A., 1988, *A&AS*, 72, 259
- Dobbie P. D., Napiwotzki R., Burleigh M. R., Barstow M. A., Boyce D. D., Casewell S. L., Jameson R. F., Hubeny I., Fontaine G., 2006, *MNRAS*, 369, 383
- Dominguez I., Chieffi A., Limongi M., Straniero O., 1999, *ApJ*, 524, 226
- Eggleton P. P., 1971, *MNRAS*, 151, 351
- Eggleton P. P., 1972, *MNRAS*, 156, 361
- Ferguson J. W., Alexander D. R., Allard F., Barman T., Bodnarik J. G., Hauschildt P. H., Heffner-Wong A., Tamanai A., 2005, *ApJ*, 623, 585
- Ferrario L., Wickramasinghe D., Liebert J., Williams K. A., 2005, *MNRAS*, 361, 1131
- Gaburov E., Lombardi J. C., Portegies Zwart S., 2008, *MNRAS*, 383, L5
- Glebbeeck E., Pols O. R., 2008, *A&A*, 488, 1017
- Glebbeeck E., Pols O. R., Hurley J. R., 2008, *A&A*, 488, 1007
- Graboske H. C., Dewitt H. E., Grossman A. S., Cooper M. S., 1973, *ApJ*, 181, 457
- Grevesse N., Noels A., 1993, in Prantzos N., Vangioni-Flam E., Casse M., eds, *Origin and Evolution of the Elements Cosmic Abundances of the Elements.* pp 14—+

- Heggie D., Hut P., 2003, *The Gravitational Million-Body Problem: A Multidisciplinary Approach to Star Cluster Dynamics*. *The Gravitational Million-Body Problem: A Multidisciplinary Approach to Star Cluster Dynamics*, by Douglas Heggie and Piet Hut. Cambridge University Press, 2003, 372 pp.
- Herwig F., 1995, in Noels A., Fraipont-Caro D., Gabriel M., Grevesse N., Demarque P., eds, *Liege International Astrophysical Colloquia Vol. 32 of Liege International Astrophysical Colloquia, The Impact of Improved Theoretical and Observational Data on the Initial-Final Mass Relation*. pp 441–+
- Hurley J. R., Pols O. R., Aarseth S. J., Tout C. A., 2005, *MNRAS*, 363, 293
- Hurley J. R., Tout C. A., Aarseth S. J., Pols O. R., 2001, *MNRAS*, 323, 630
- Hut P., Shara M. M., Aarseth S. J., Klessen R. S., Lombardi Jr. J. C., Makino J., McMillan S., Pols O. R., Teuben P. J., Webbink R. F., 2003, *New Astronomy*, 8, 337
- Iben Jr. I., 1975, *ApJ*, 196, 525
- Iben Jr. I., Fujimoto M. Y., MacDonald J., 1992, *ApJ*, 388, 521
- Iglesias C. A., Rogers F. J., 1996, *ApJ*, 464, 943
- Iliadis C., 2007, *Nuclear Physics of Stars*. *Nuclear Physics of Stars*, by Christian Iliadis. ISBN 978-3-527-40602-9. Published by Wiley-VCH Verlag, Weinheim, Germany, 2007.
- Irwin A. W., 1987, *A&A*, 182, 348
- Itoh N., Hayashi H., Nishikawa A., Kohyama Y., 1996, *ApJS*, 102, 411
- Kovetz A., 1998, *ApJ*, 495, 401
- Kovetz A., 1999, *Phys. Rep.*, 311, 383
- Kovetz A., Shaviv G., 1970, *A&A*, 8, 398
- Lamers H. J. G. L. M., 1981, *ApJ*, 245, 593
- Lombardi Jr. J. C., Warren J. S., Rasio F. A., Sills A., Warren A. R., 2002, *ApJ*, 568, 939
- Makino J., Taiji M., Ebisuzaki T., Sugimoto D., 1997, *ApJ*, 480, 432
- Meng X., Chen X., Han Z., 2007, *ArXiv e-prints*, 710
- Mihalas D., 1978, *Stellar atmospheres*, 2nd edition,. San Francisco, W. H. Freeman and Co., 1978. 650 p.
- Morel P., Provost J., Berthomieu G., 2000, *A&A*, 353, 771
- Nieuwenhuijzen H., de Jager C., 1990, *A&A*, 231, 134
- Pols O. R., Schroder K.-P., Hurley J. R., Tout C. A., Eggleton P. P., 1998, *MNRAS*, 298, 525

- Pols O. R., Tout C. A., Eggleton P. P., Han Z., 1995, *MNRAS*, 274, 964
- Portegies Zwart S. F., Hut P., McMillan S. L. W., Makino J., 2004, *MNRAS*, 351, 473
- Portegies Zwart S. F., McMillan S. L. W., Hut P., Makino J., 2001, *MNRAS*, 321, 199
- Rakavy G., Shaviv G., Zinamon Z., 1967, *ApJ*, 150, 131
- Reimers D., 1975, *Memoires de la Societe Royale des Sciences de Liege*, 8, 369
- Reiter J., Walsh L., Weiss A., 1995, *MNRAS*, 274, 899
- Schröder K.-P., Cuntz M., 2005, *ApJL*, 630, L73
- Schröder K.-P., Cuntz M., 2007, *A&A*, 465, 593
- Serenelli A. M., Fukugita M., 2007, *ApJS*, 172, 649
- Shaviv G., Kovetz A., 1972, *A&A*, 16, 72
- Sills A., Lombardi Jr. J. C., Baily C. D., Demarque P., Rasio F. A., Shapiro S. L., 1997, *ApJ*, 487, 290
- Stancliffe R. J., 2006, *MNRAS*, 370, 1817
- Tatum J. B., 1966, *Publications of the Dominion Astrophysical Observatory Victoria*, 13, 1
- Turcotte S., Richer J., Michaud G., Iglesias C. A., Rogers F. J., 1998, *ApJ*, 504, 539
- Umeda H., Nomoto K., 2008, *ApJ*, 673, 1014
- Weidemann V., 2000, *A&A*, 363, 647
- Williams K. A., 2007, in Napiwotzki R., Burleigh M. R., eds, *Astronomical Society of the Pacific Conference Series Vol. 372, A New Look at the Empirical Initial–Final Mass Relation*. p. 85

Table 2. Timescales and final WD masses and compositions - Populations I and II canonical sequences

M_i	M_f	Pop. I ($Z = 0.01$)			WD	Pop. II ($Z = 0.001$)			WD
		τ_{MS}	τ_{RGB}			M_f	τ_{MS}	τ_{RGB}	
0.25	0.25	8.70E+11	1.58E+10		He	0.25	5.41E+11	1.77E+10	He
0.50	0.41	1.18E+11	6.38E+09		He	0.46	9.10E+10	4.54E+09	He
0.80	0.53	1.98E+10	1.91E+09		CO	0.54	1.44E+10	1.18E+09	CO
1.00	0.55	8.00E+09	1.24E+09		CO	0.56	6.02E+09	7.51E+08	CO
2.00	0.60	7.43E+08	8.70E+07		CO	0.62	5.04E+08	1.00E+08	CO
3.00	0.64	2.56E+08	2.75E+07		CO	0.74	2.00E+08	2.18E+07	CO
4.00	0.80	1.25E+08	9.97E+06		CO	0.92	1.10E+08	9.16E+06	CO
5.00	0.92	6.88E+07	5.80E+06		CO	0.99	7.00E+07	4.84E+06	CO
6.00	0.97	4.52E+07	3.48E+06		CO	1.05	4.91E+07	2.86E+06	CO
7.00	1.00	3.27E+07	2.08E+06		CO	1.15	3.34E+07	2.15E+06	CO
8.00	1.05	2.44E+07	1.82E+06		CO	1.20	2.60E+07	1.51E+06	ONeMg
9.00	1.16	2.23E+07	1.11E+06		ONeMg	1.24	1.63E+07	1.26E+06	ONeMg

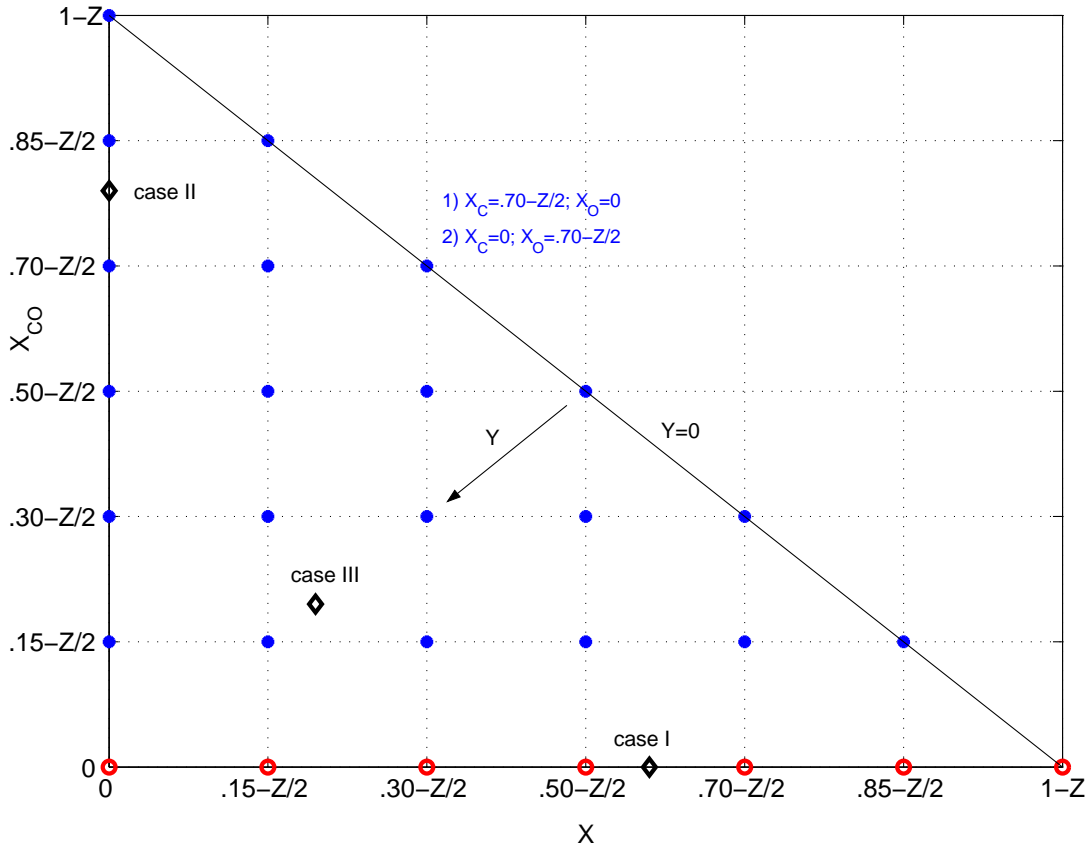


Figure 1. A Schematic representation of our set of 49 opacity tables—spanning a triangular shape in $[X, X_{CO}]$ space—in between which interpolations are performed for a given metallicity Z . The 7 open circles along the x-axis denote the 7 tables for zero CO excesses. Each point within the remaining 21 dots represents two tables: the excess being completely in carbon for one and completely in oxygen for the other (such as noted as example for the $(X = .30 - Z/2, X_{CO} = .70 - Z/2)$ position). The hypotenuse of the triangle relates to zero helium mass fraction ($Y = 0$).

This paper has been typeset from a $\text{\TeX}/\text{\LaTeX}$ file prepared by the author.

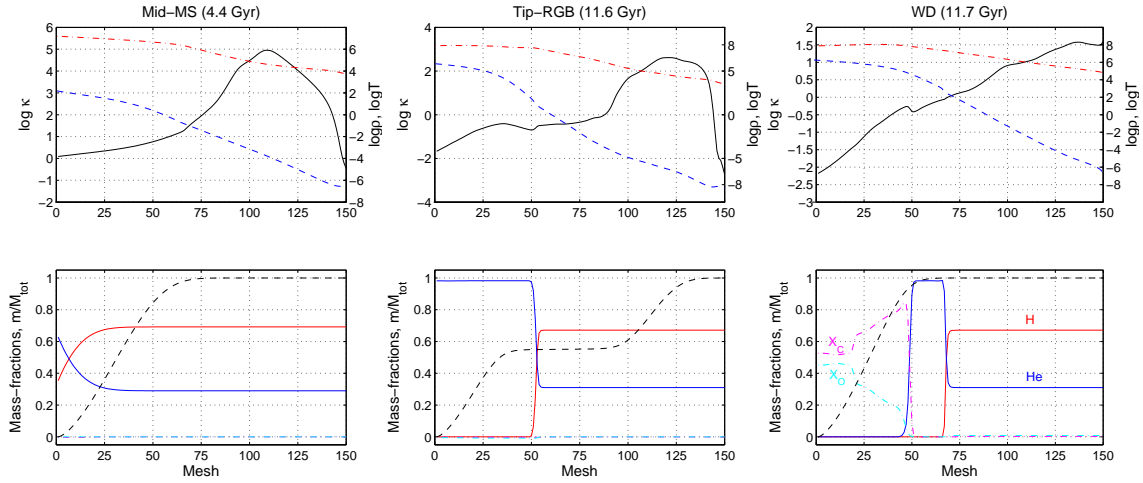


Figure 2. Profiles of internal structure at three snapshots during evolution of a solar model - Mid-MS (left), tip of RGB (middle) and cooling WD (right). Top panels display profiles of opacity (solid black), density (dashed blue) and temperature (dot-dashed red). Bottom panels display internal composition in terms of elemental mass fractions - hydrogen (solid red), helium (solid blue), and excesses of carbon and oxygen (dot-dashed magenta and cyan, respectively; values for the excesses are representing closely those of total C and O mass fractions). Dashed black plots display m/M_{tot} ; M_{tot} equal 1.00, 0.81 and $0.55 M_{\odot}$ for the three profiles, left to right, respectively. Only in the rightmost panel are the carbon and oxygen excesses non-zero (post core helium burning).

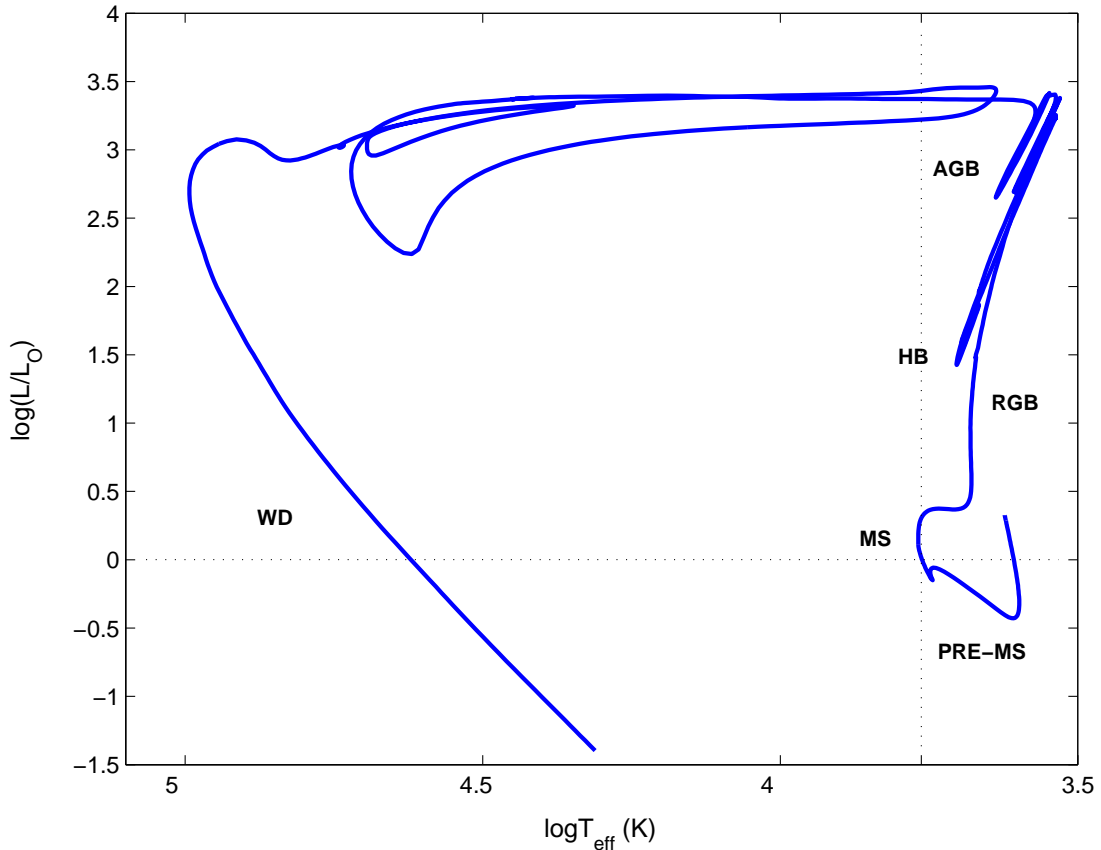


Figure 3. Solar model HRD - A complete evolutionary track as obtained for $1M_{\odot}$, $Y = 0.29$, $Z = 0.018$ and mixing-length parameter $\alpha = 2.5$.

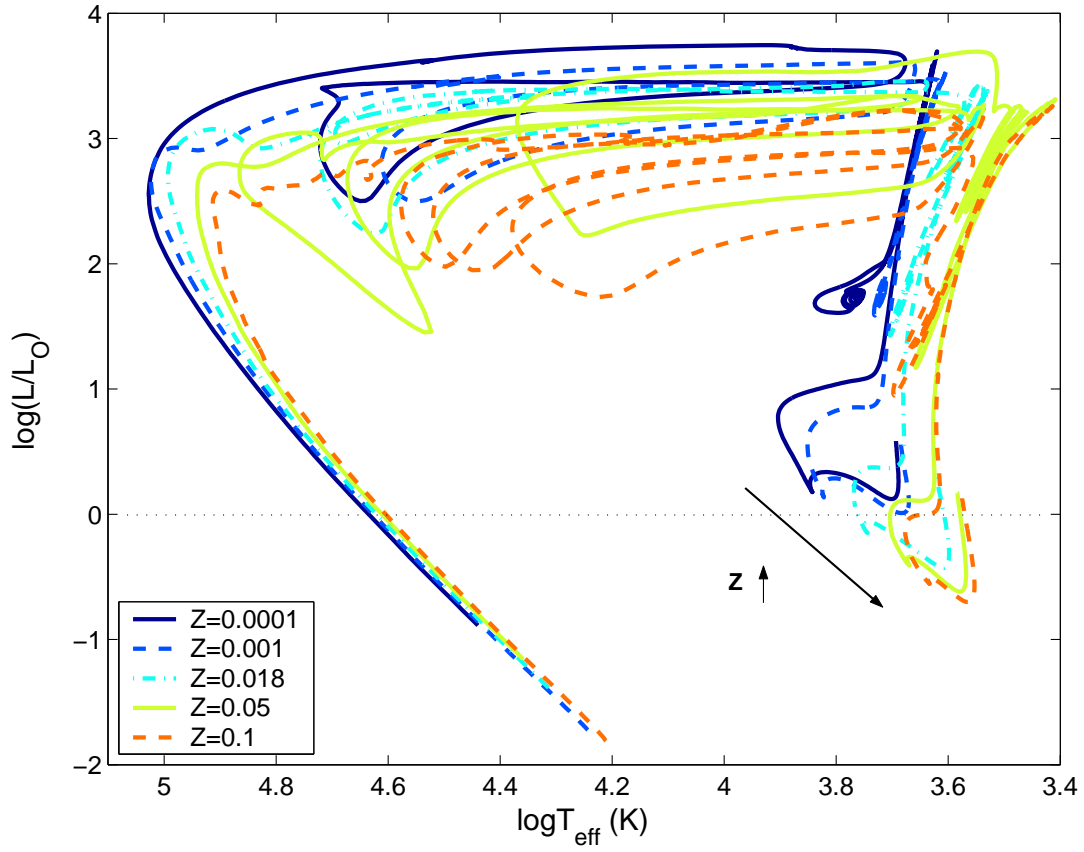


Figure 4. Complete tracks on HRD for various metallicities $Z = 0.0001$ to 0.1 for $1M_{\odot}$. MS effective temperatures and luminosities decrease with increasing metallicity; consequently - durations of MS increase (by a factor of over 3 from the lowest value of Z to the highest).

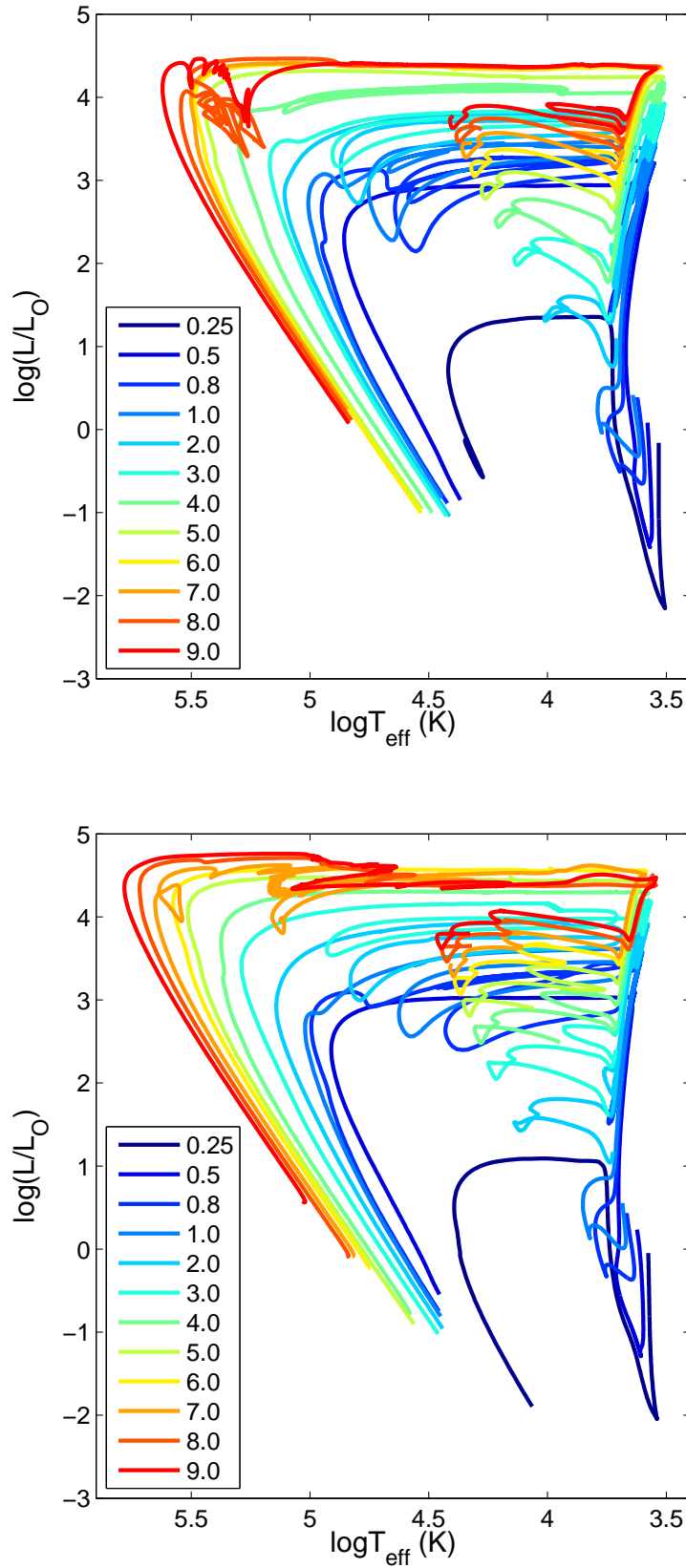


Figure 5. Complete tracks on HRD—Pre-MS to cooling WD—for initial (ZAMS) masses in the range 0.25 to 9.0 M_{\odot} . Top: population I models ($Z = 0.01$, $Y = 0.28$). Bottom: population II models ($Z = 0.001$, $Y = 0.24$).

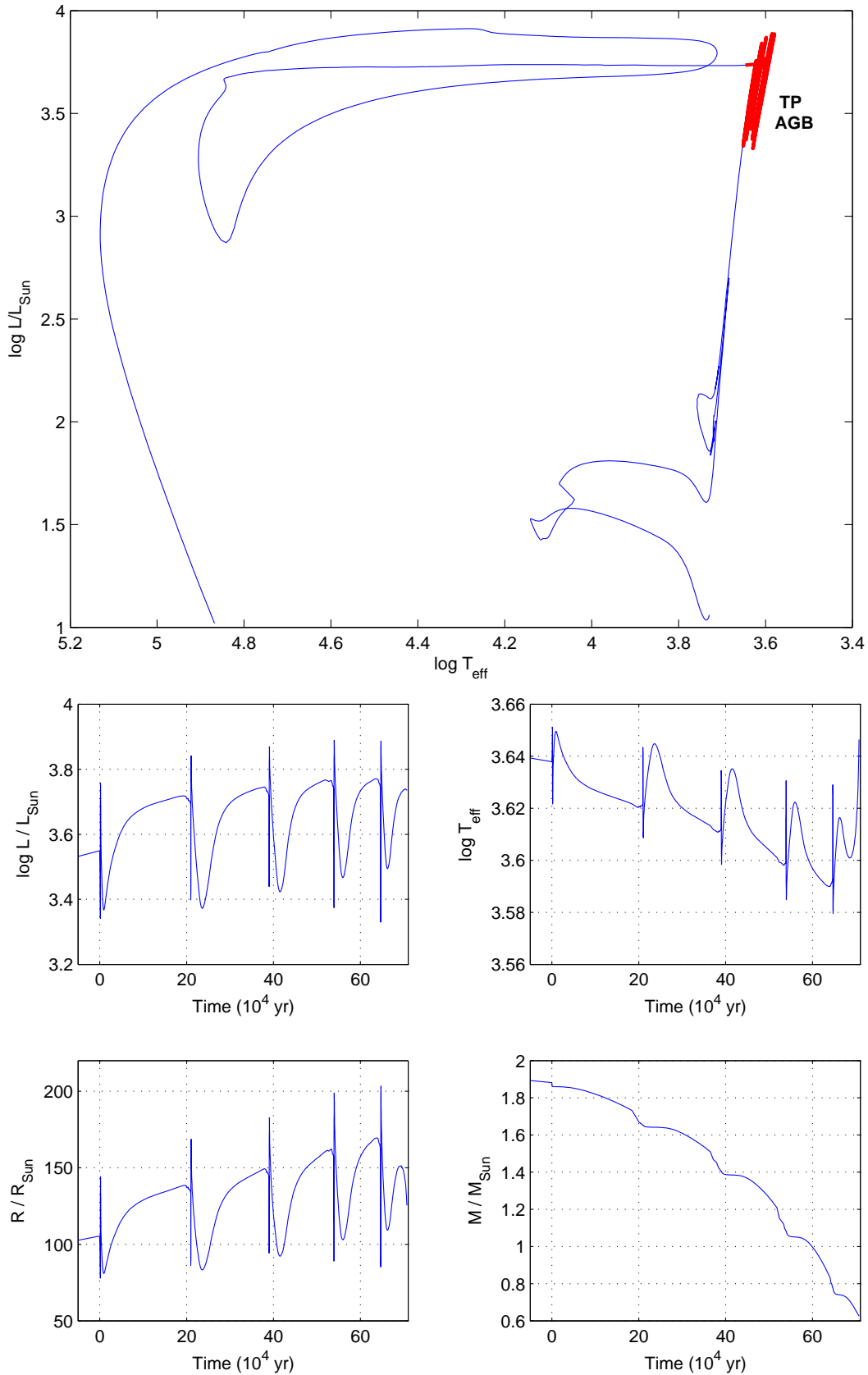


Figure 6. Thermal pulses during TP-AGB for the $2 M_{\odot}$ Pop.II ($Z = 0.001$, $Y = 0.24$) model. Top: complete track on HRD; plotted in thick red is the TP-AGB phase, for which the bottom panels are plotted. Bottom: Evolution of various characteristics during the thermal pulses phase.

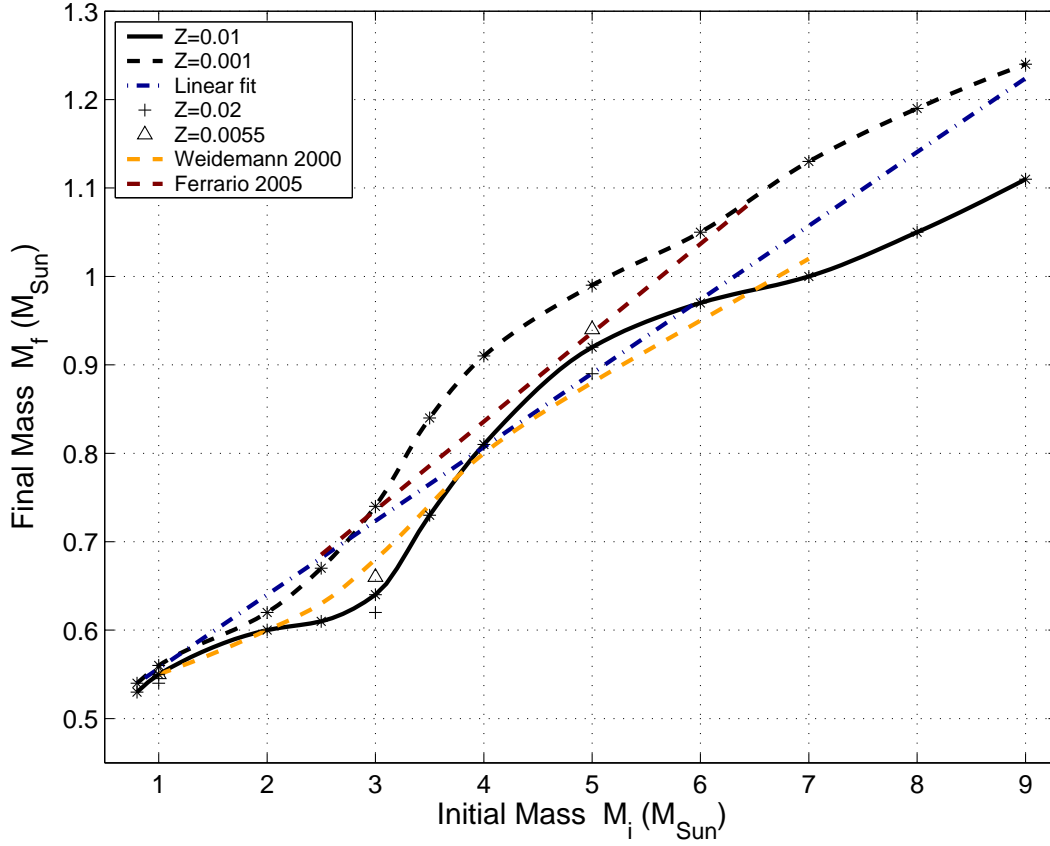


Figure 7. IFMR - Final vs. initial masses as obtained for both our Pop.I (solid black) and Pop.II (dashed black) evolutionary sequences, for initial masses in the range 0.8 to 9 M_{\odot} . The solid blue line is a linear fit to all values (Pop.I and II). We show for comparison the revised Weidemann (2000) semi-empirical relationship (M_i in the range 1 to 7 M_{\odot}), as well as the empirical linear relation by Ferrario et al. (2005) (M_i in the range 2.5 to 6.5 M_{\odot}). See text for details.

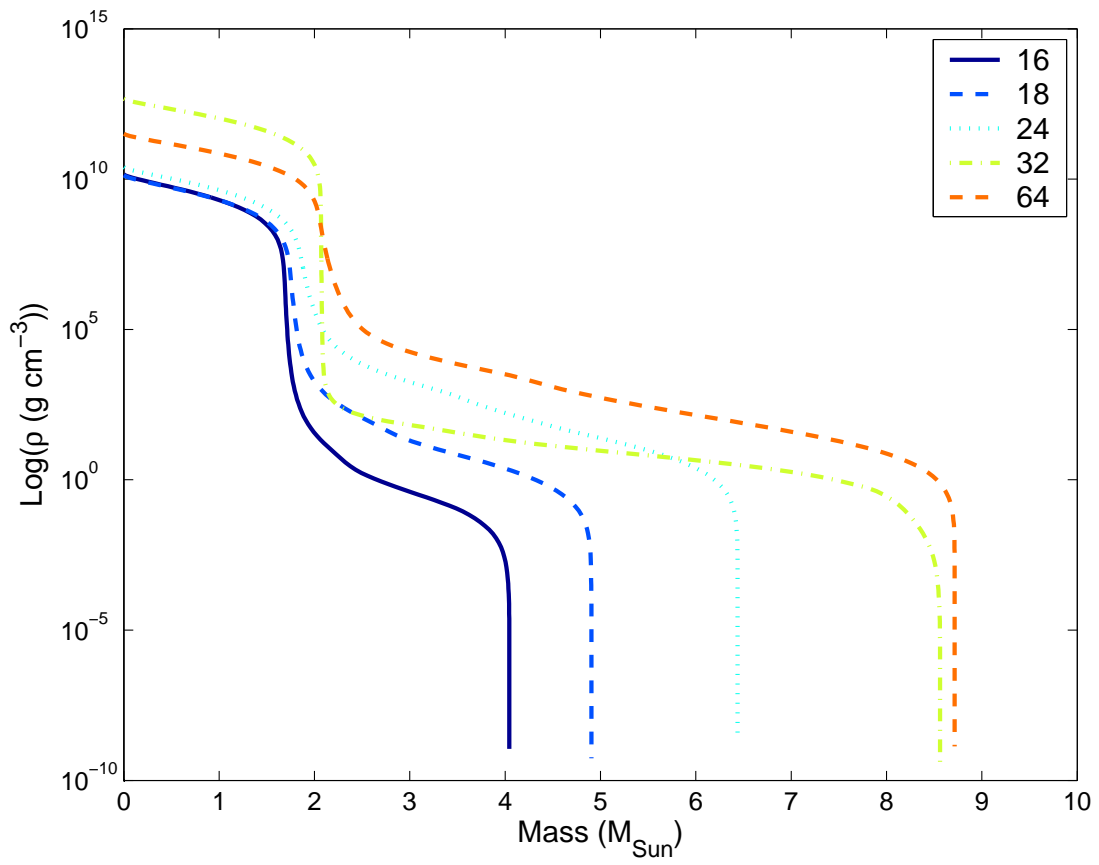


Figure 8. Density profiles in massive stars (Pop.I) with collapsed cores (legend shows initial masses).

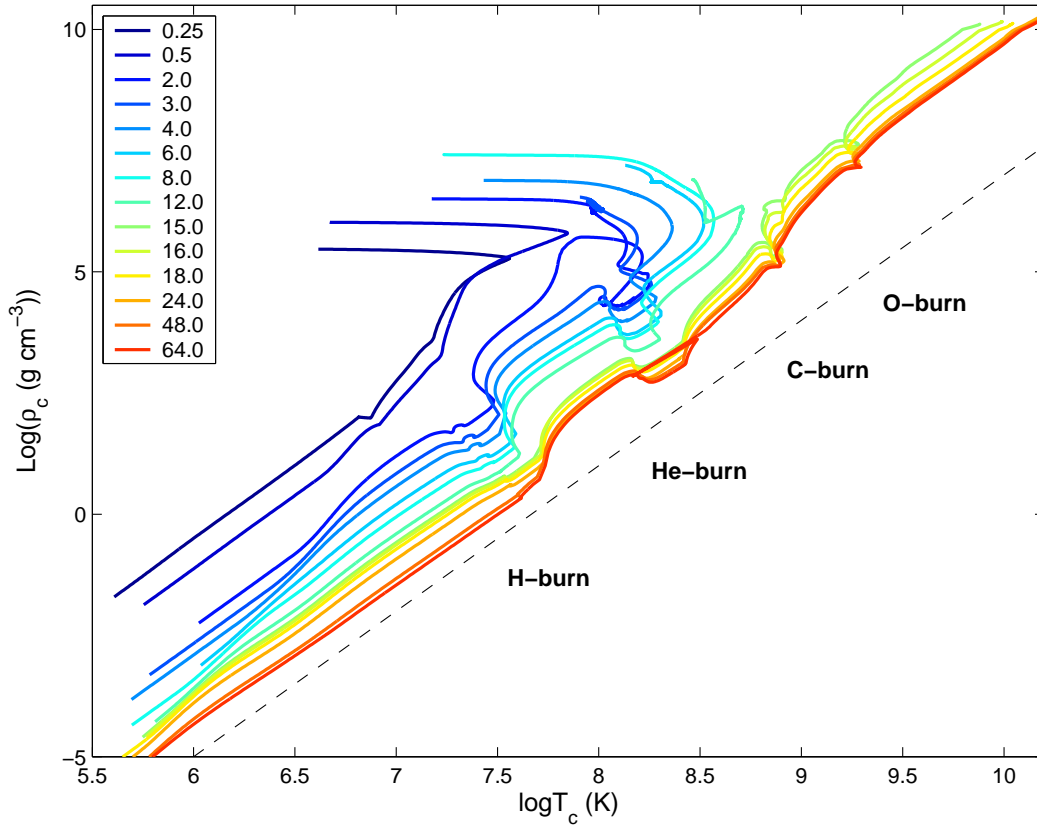


Figure 9. Evolution of the central stellar density and temperature for Pop.I ($Z = 0.018$) models in the range $0.25 - 64 M_\odot$. Dotted line has a slope of 3 (as obtained for the $\text{log } \rho_c - \text{log } T_c$ relation of hydrostatic equilibrium under ideal gas law). Nuclear burning phases are marked along the tracks.

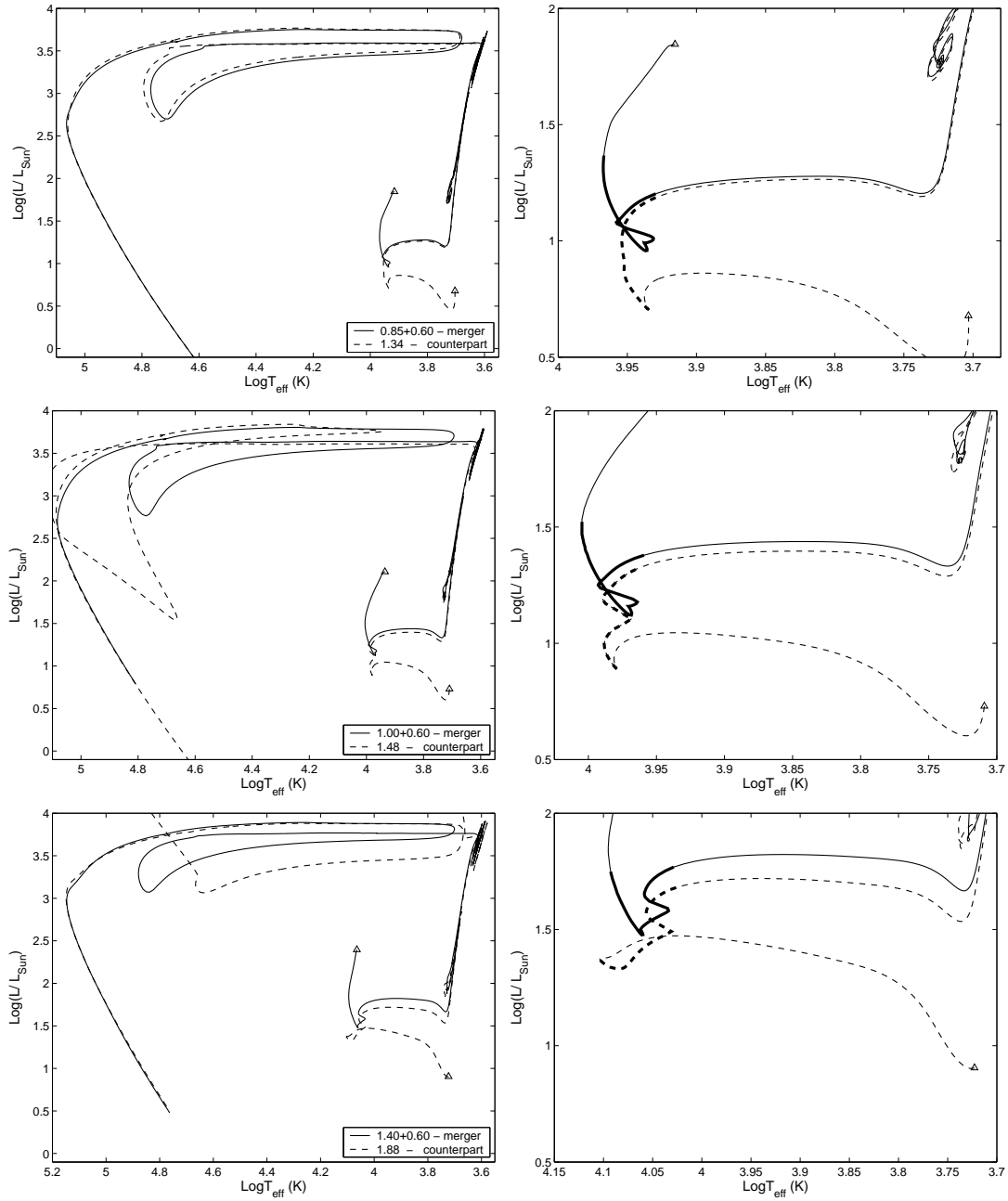


Figure 10. Non-canonical evolution - evolutionary tracks on HRD of the three merger products (solid) of low-mass MS parent stars, with comparison to their canonical counterparts - 'normal' initial configurations of equal mass (dashed). Triangles denote starting points for both the canonical and non-canonical evolutionary tracks. Panels on the right are a blow-up of the (MS,early-RGB) regions; thicker solid and dashed sections denote the extent of MS evolution phase.

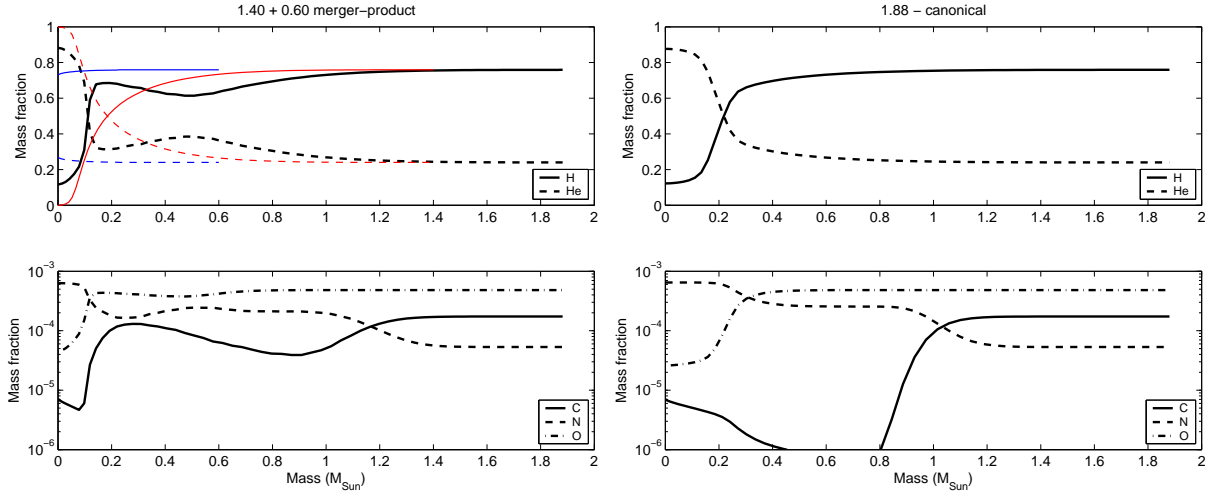


Figure 11. Left: Composition profiles (top: H,He; bottom: C,N,O) of the $1.40 + 0.60 M_{\odot}$ merger-product, as obtained from the Make Me A Star ver 1.6 package for a head-on collision (see text), right after the configuration has been hydrostatically relaxed by our code – ready to be evolved. Shown in thin lines at the top panel are the H and He profiles of the $1.40 M_{\odot}$ (red) and $0.60 M_{\odot}$ (blue) parent stars, evolved to an age of 1.5 Gyr. Right: similar profiles for the canonical counterpart – a ‘normal’ $1.88 M_{\odot}$ star – when its central He mass fraction equals that of the merger product.